https://doi.org/10.3847/1538-4365/ab1658

Core Cosmology Library: Precision Cosmological Predictions for LSST

Nora Elisa Chisari[1], David Alonso[1,2], Elisabeth Krause[3,4], C. Danielle Leonard[5], Philip Bull[6,7], Jérémy Neveu[8],
Antonio Villarreal[9], Sukhdeep Singh[5,10], Thomas McClintock[11], John Ellison[12], Zilong Du[12], Joe Zuntz[13],
Alexander Mead[14], Shahab Joudaki[1], Christiane S. Lorenz[1], Tilman Tröster[13], Javier Sanchez[15], Francois Lanusse[5],
Mustapha Ishak[16], Renée Hlozek[17], Jonathan Blazek[18,19], Jean-Eric Campagne[8], Husni Almoubayyed[5], Tim Eifler[3,20],
Matthew Kirby[11], David Kirkby[15], Stéphane Plaszczynski[8], Anže Slosar[21], Michal Vrastil[22], and Erika L. Wagoner[11]

(LSST Dark Energy Science Collaboration)

[1] Department of Physics, University of Oxford, Denys Wilkinson Building, Keble Road, Oxford OX1 3RH, UK
[2] School of Physics and Astronomy, Cardiff University, The Parade, Cardiff, CF24 3AA, UK
[3] Steward Observatory/Department of Astronomy, University of Arizona, 933 North Cherry Avenue, Tucson, AZ 85721, USA
[4] Kavli Institute for Particle Astrophysics and Cosmology, Stanford, CA 94305-4085, USA
[5] McWilliams Center for Cosmology, Department of Physics, Carnegie Mellon University, Pittsburgh, PA 15213, USA
[6] School of Physics & Astronomy, Queen Mary University of London, 327 Mile End Road, London E1 4NS, UK
[7] Department of Astronomy, University of California Berkeley, Berkeley, CA 94720, USA
[8] Laboratoire de l'Accélérateur Linéaire, Université Paris-Sud, CNRS/IN2P3, Université Paris-Saclay, Orsay, France
[9] Argonne National Laboratory, Argonne, IL 60439, USA
[10] Berkeley Center for Cosmological Physics and Department of Physics, University of California, Berkeley, CA, USA
[11] Department of Physics, University of Arizona, Tucson, AZ 85721, USA
[12] Department of Physics and Astronomy, University of California, Riverside, CA 92521, USA
[13] Institute for Astronomy, Royal Observatory Edinburgh, Edinburgh EH9 3HJ, UK
[14] Department of Physics and Astronomy, University of British Columbia, 6224 Agricultural Road, Vancouver, BC V6T 1Z1, Canada
[15] Department of Physics and Astronomy, University of California, Irvine, CA 92697, USA
[16] Department of Physics, The University of Texas at Dallas, Richardson, TX 75083, USA
[17] Dunlap Institute for Astronomy and Astrophysics & Department for Astronomy and Astrophysics, University of Toronto, ON M5S 3H4, Canada
[18] Center for Cosmology and Astroparticle Physics, Ohio State, Columbus, OH 43210, USA
[19] SNSF Ambizione, Laboratory of Astrophysics, École Polytechnique Fédérale de Lausanne (EPFL), 1290 Versoix, Switzerland
[20] Jet Propulsion Laboratory, California Institute of Technology, Pasadena, CA 91109, USA
[21] Brookhaven National Laboratory, Physics Department, Upton, NY 11973, USA
[22] Institute of Physics CAS, Prague, 182 21, Czech Republic

Abstract

The Core Cosmology Library (CCL) provides routines to compute basic cosmological observables to a high degree of accuracy, which have been verified with an extensive suite of validation tests. Predictions are provided for many cosmological quantities, including distances, angular power spectra, correlation functions, halo bias, and the halo mass function through state-of-the-art modeling prescriptions available in the literature. Fiducial specifications for the expected galaxy distributions for the Large Synoptic Survey Telescope (LSST) are also included, together with the capability of computing redshift distributions for a user-defined photometric redshift model. A rigorous validation procedure, based on comparisons between CCL and independent software packages, allows us to establish a well-defined numerical accuracy for each predicted quantity. As a result, predictions for correlation functions of galaxy clustering, galaxy–galaxy lensing, and cosmic shear are demonstrated to be within a fraction of the expected statistical uncertainty of the observables for the models and in the range of scales of interest to LSST. CCL is an open source software package written in C, with a Python interface and publicly available at https://github.com/LSSTDESC/CCL.

Key words: cosmology: theory – dark energy – large-scale structure of universe

1. Introduction

Starting in the next decade, large-scale galaxy surveys will drive a new era of high-precision cosmology (Green et al. 2011; Laureijs et al. 2011; LSST Dark Energy Science Collaboration 2012). One of their main goals is to answer the question of the origin of cosmic acceleration, in other words, to elucidate the nature of "dark energy," broadly understood as a family of potential models: from a cosmological constant to a dynamical field and modifications of gravity (see for example Carroll 2001; Padmanabhan 2003; Peebles & Ratra 2003; Copeland et al. 2006; Ishak 2007; Weinberg et al. 2013 and references therein). These data will also allow us to shed light on a number of open questions in fundamental physics, such as the nature of dark matter (Feng 2010; Porter et al. 2011), the mass of neutrinos (Wong 2011; Lesgourgues & Pastor 2012;

Allison et al. 2015), or the level of primordial non-Gaussianity (Dalal et al. 2008; Desjacques & Seljak 2010).

High-precision constraints on dark energy models will be achieved by probing at the same time the expansion and growth history of the universe over a long redshift baseline. For this purpose, it will be crucial to combine measurements of multiple cosmological probes: weak and strong gravitational lensing, the clustering of galaxies, distances to supernovae, and the abundance, clustering, and gravitational lensing of galaxy clusters. Current weak-lensing surveys, such as the Dark Energy Survey[23] and the Kilo Degree Survey,[24] have started to take this approach already (Krause et al. 2017; Abbott et al. 2018; Joudaki et al. 2018; van Uitert et al. 2018). From a theoretical

---

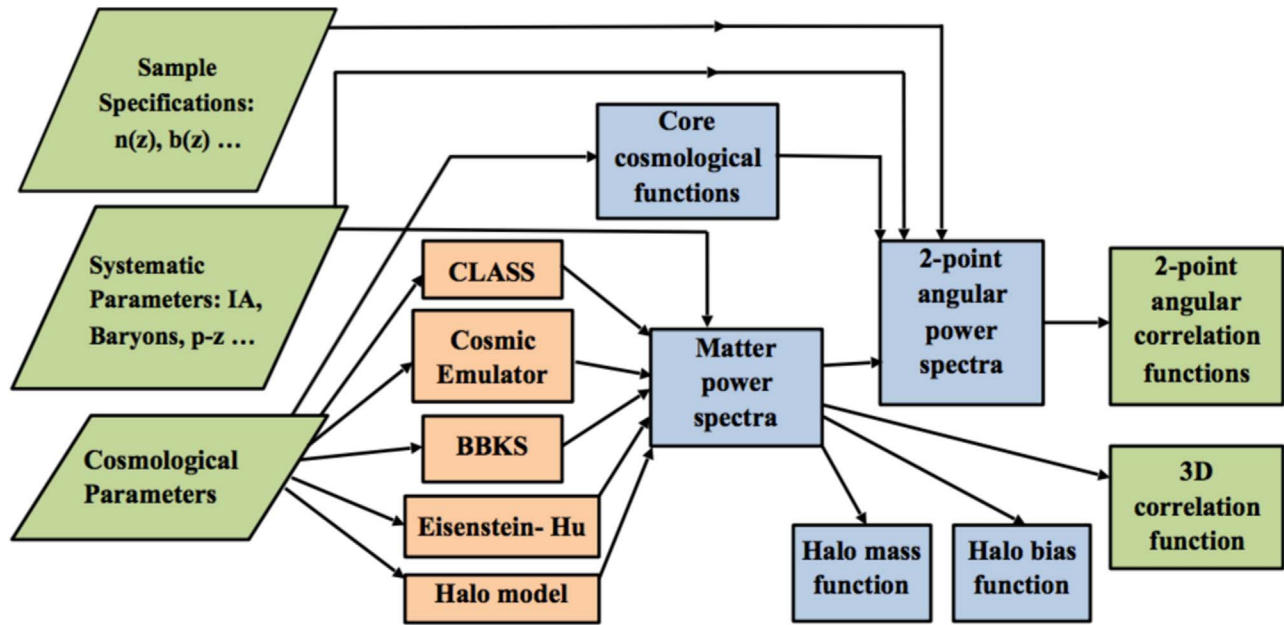[23] https://www.darkenergysurvey.org
[24] http://kids.strw.leidenuniv.nl

Figure 1. CCL structure flowchart. CCL is written in C with a Python interface. CCL routines calculate basic cosmological functions such as the Hubble function, density parameters, distances, and growth function. The library uses various methods to compute the matter power spectrum, including CLASS, the "Cosmic Emulator" developed by Lawrence et al. (2017), and other common approximations. CCL computes two-point angular power spectra and correlation functions from various probes, including typical astrophysical systematics and accounting for user-provided or precoded survey specifications.

perspective, there are two challenges faced by the next generation of galaxy surveys.

First, we need to ensure that all probes are modeled accurately from a physical point of view, including cosmological, astrophysical, and observational effects, to avoid potential biases in the final cosmological results. In the context of weak gravitational lensing, for example, phenomena that can lead to biases include the impact of baryons on the distribution of matter and the intrinsic alignments of galaxies (e.g., Semboloni et al. 2011; van Daalen et al. 2011; Troxel & Ishak 2015; Krause et al. 2016; Blazek et al. 2017; Chisari et al. 2018). In the context of galaxy clustering, the most relevant astrophysical systematic is the galaxy–matter bias relation on small scales (Zhao et al. 2013; Desjacques et al. 2018). Effects such as the magnification of number counts and redshift space distortions need to be included in the models as well (Alonso & Ferreira 2015; Ghosh et al. 2018).

Second, even standard cosmological quantities in the simplest models, such as distances in a ΛCDM cosmology, have to be predicted to a validated high degree of numerical accuracy. Achieving this objective is not trivial, as computing these quantities generally requires, for example, numerical integration or interpolation, both of which are prone to numerical error.

Commonly used, publicly available, cosmological prediction tools are astropy[25] (Astropy Collaboration et al. 2013), NumCosmo[26] (Doux et al. 2018), and CAMB[27] (Lewis & Bridle 2002). However, none of these meets all the necessary capabilities for cosmological analysis with the next generation of dark energy experiments.

Faced with these challenges, the Dark Energy Science Collaboration (DESC), one of the science collaborations of the Large Synoptic Survey Telescope (LSST), has built a comprehensive software tool that satisfies the needs of the next generation of cosmological analysis: the Core Cosmology Library[28] (CCL). CCL is a software library providing the infrastructure to make theoretical predictions that are validated to a well-documented high degree of numerical accuracy for the purpose of constraining cosmology. In the context of this work, we establish the accuracy of CCL predictions by comparing them to predictions from external packages. Thus, what we quantify is the level of agreement between independent pipelines.

CCL computes standard cosmological functions including the Hubble parameter, cosmological distances, density parameters, the halo mass function, halo bias, and linear growth functions. It calculates the matter power spectrum using various methods including common approximations, by calling external software such as CLASS (Blas et al. 2011), or emulators, such as the "Cosmic Emulator" of Lawrence et al. (2017). It computes two-point angular power spectra and correlation functions from various probes, going beyond the Limber approximation. While CCL incorporates state-of-the-art models available in the literature, this manuscript is mainly concerned with documenting their implementation and numerical accuracy, but does not address the physical accuracy of each model, for which we point the reader to the relevant references in the following sections. To our knowledge, no other adaptable, up-to-date, and publicly available software tool for state-of-the-art cosmological predictions has undergone such a rigorous validation process as described in this manuscript.

CCL's overall structure is illustrated in Figure 1. Our implementation has support for spatially flat and curved Λ-Cold Dark Matter (ΛCDM) cosmologies and wCDM cosmologies with

---

[25] http://www.astropy.org
[26] https://numcosmo.github.io
[27] https://camb.info

[28] Publicly available at https://github.com/LSSTDESC/CCL.

the option of using a time-dependent equation of state. It also allows for cosmologies with multiple massive neutrino species and can be linked to external software for modified gravity predictions (hi_CLASS; Zumalacárregui et al. 2017). While CCL was built with LSST in mind, the goal is to produce a publicly available, user-friendly, well-documented, adaptable software that can be used in any theoretical modeling work in cosmology. This manuscript describes version 1.0.0 of the library.

The validation procedure to assess the numerical accuracy of each CCL feature is key in this work. We compare the CCL evaluation of each observable or function to an independent implementation from a stand-alone software package. For each prediction, we define an accuracy metric that surpasses our expected needs for accurate cosmological constraints, and document the results obtained in this manuscript. Ultimately, the numerical uncertainties in the different CCL functions propagate to our predictions for correlation functions, which we expect to be one of the main summary statistics used in the LSST cosmology analyses (similarly to current DES and KiDS efforts). Hence, our overall goal in this work is to demonstrate that correlation functions obtained by CCL are accurate to within a fraction of the expected observational uncertainties for the models and in the range of scales of interest to LSST. In addition, we ensure that any prediction of the two-point statistics of the distribution of matter, necessary for predicting cross-correlations between probes, has a well-established accuracy.

This paper is organized as follows. Section 2 describes the cosmological models and observables supported by CCL. In Section 3, we describe the details of the implementation of the quantities introduced in Section 2. Section 4 provides details of the validation procedure, the tests performed, and the accuracy achieved. Section 5 gives brief guidelines for using CCL, although we direct the reader to the software online repository, documentation, and user manual for further information. We conclude in Section 6 with an outlook toward the integration of CCL in the LSST DESC pipelines, and we outline future additions to the software.

2. Cosmological Models and Observables

The overarching goal of CCL is to allow seamless integration of different cosmological models of interest to LSST. The cosmological models assume a homogeneous and isotropic spacetime metric, and an inflationary model for the primordial universe described by a power law with spectral index n_s, and amplitude A_s defined at a pivot scale of $k_0 = 0.05 \, \mathrm{Mpc}^{-1}$. The cosmological components include the matter density parameter Ω_m, which is the sum of the baryonic component Ω_b and the cold dark matter component Ω_c; the dark energy density[29] Ω_Λ; the radiation density Ω_γ (excluding neutrinos); the curvature density Ω_K; and the neutrino density of both massless and massive neutrinos, given by $\Omega_{\nu,\mathrm{rel}}$ and $\Omega_{\nu,\mathrm{m}}$, respectively. Unless otherwise specified, we refer to these densities at the present. The current expansion rate is given by the Hubble constant, $H_0 = 100 \, h \, \mathrm{km \, s^{-1} \, Mpc^{-1}}$. The normalization of the density fluctuations is established either in terms of A_s or in terms of the rms variance in spheres of $8 \, h \, \mathrm{Mpc}^{-1}$ today, σ_8.

The following set of models is supported in CCL:

1. Flat ΛCDM cosmology governed by the parameters Ω_b, Ω_m, H_0, n_s, A_s, or σ_8, and a cosmological constant dark energy model with equation of state $w = -1$.
2. The Chevallier–Polarski–Linder (CPL) model for dark energy, which adopts the following parameterization for w as a function of the scale factor, a (Chevallier & Polarski 2001 and Linder 2003),

$$w(a) = w_0 + w_a(1 - a). \quad (1)$$

We note that models with constant w are simply a subset of the above, where $w_a = 0$.
3. Nonzero curvature (K), so that the curvature density parameter $\Omega_K = 1 - \sum_i \Omega_i$, where i refers to each of the density components.
4. Extrarelativistic species, contributing to N_{eff} (the effective number of neutrinos).
5. Massive neutrinos specified by either the sum of their masses Σm_ν (which maps onto the density parameter $\Omega_{\nu,\mathrm{m}}$ above) or by the individual masses of each of the three neutrino species. This feature is allowed alongside nonzero curvature, extrarelativistic species, and evolving dark energy.
6. An arbitrary, user-defined modified growth function (see description in Section 2.2). This can be combined with a model that otherwise contains nonzero curvature and evolving dark energy.

In the particular case of cosmologies with massive neutrinos, if the user specifies a sum of masses, Σm_ν, CCL will by default split Σm_ν into three neutrino masses consistent with the normal hierarchy (see, e.g., Lattanzi & Gerbino 2017 for a review). However, the user can alternatively ask for Σm_ν to be split either into masses consistent with the inverted hierarchy or into equal masses. Each neutrino species is then checked for whether it is nonrelativistic (massive) at $z = 0$, and this information is used in combination with the user-provided value of N_{eff} to set the number of relativistic neutrino species.

The following subsections describe the cosmological predictions implemented in CCL. Not all CCL features are available for the models described in this section. For a guide to which predictions are available for each model, see Table 1. Note that if users install their own version of the CLASS software (for example, hi_CLASS; Zumalacárregui et al. 2017), CCL can then make predictions for a more extended set of cosmologies. Users should take care to understand the validity of the CCL assumptions for their own models.

2.1. Background Cosmology

The models that are specified above map directly onto cosmological observables such as the expansion rate of the universe, which is parameterized through the Hubble parameter as

$$\frac{H(a)}{H_0} = a^{-3/2}(\Omega_m + \Omega_\Lambda a^{-3(w_0 + w_a)} \exp[3w_a(a - 1)]$$
$$+ \Omega_K a + (\Omega_\gamma + \Omega_{\nu,\mathrm{rel}}) a^{-1} + \tilde{\Omega}_{\nu,\mathrm{m}}(a) a^3)^{\frac{1}{2}} \quad (2)$$

and is a function of the scale factor and of the energy density in the different components today. In this expression, we have assumed the CPL parameterization described above for the dark energy equation of state, and we have defined $\tilde{\Omega}_{\nu,\mathrm{m}}(a) \equiv \rho_{\mathrm{crit}}^{-1} \rho_{\nu,\mathrm{m}}(a)$ as the fractional energy density of massive

---

[29] While we adopt Ω_Λ as the notation, this quantity also represents the dark energy density in the case where dark energy is described by a dynamical field.

Table 1
Cosmologies Implemented in CCL and Observables Supported for Each of Them

| | Flat | | ΛCDM + | |
Observable/Model	ΛCDM	ΛCDM+K	m_ν	wCDM
Distances	✓	✓	✓	✓
Growth function	✓	✓	✗	✓
$P_m(k, z)$	✓	✓	✓	✓
Halo mass function	✓	✓	✗	✓
C_l, number counts	✓	✗	✗	✓
C_l, weak/CMB lensing	✓	✗	✓	✓
Correlation function	✓	✗	✓	✓
Halo model	✓	✓	✗	✓

Note. Note that the only reason why angular power spectra appear not to be supported in nonflat cosmologies is that the hyperspherical Bessel functions are currently not implemented, although their impact is fairly limited. Likewise, number counts power spectra are strictly not supported in the presence of massive neutrino cosmologies, due to the scale-dependent growth rate that affects the redshift-space distortion term, even though the impact of this is also small for wide tomographic bins. The halo model can make matter power spectrum predictions for all cosmologies, but should not be used for massive neutrino models because the current version does not distinguish between cold matter, which is relevant for clustering, and all matter. Finally, we note that CCL can make predictions for the growth of perturbations for some modified gravity models through a user-defined $\Delta f(a)$ as detailed in Section 2.2, and that other extensions are supported via the integration of external modified gravity codes.

neutrinos as a function of time, where $\rho_{\rm crit}$ is the critical density of the universe today.

In general, the density parameter $\Omega_X(a)$ of a given species X at a given time is defined in terms of the physical background densities $\bar{\rho}_X(a)$ via $\Omega_X(a) \equiv \rho_{\rm crit}^{-1}(a) \bar{\rho}_X(a)$, where the critical density of the universe at a given time is

$$\rho_{\rm crit}(a) = (8\pi G)^{-1} 3 c^2 H^2(a) = \rho_{\rm crit} H_0^{-2} H^2(a). \quad (3)$$

As an example, the physical density of matter is given by

$$\bar{\rho}_m(a) = \bar{\rho}_m a^{-3} = \rho_{\rm crit} \Omega_m a^{-3}, \quad (4)$$

and its density parameter is

$$\Omega_m(a) = \Omega_m H_0^2 a^{-3} H^{-2}(a). \quad (5)$$

Moreover, CCL allows for comoving physical densities $\bar{\rho}_{X,{\rm com}}(a) = \bar{\rho}_X(a) a^3$ to be extracted, which in the case of matter reduces to a time-independent $\bar{\rho}_{m,{\rm com}} = \rho_{\rm crit} \Omega_m$. We include bars for ρ_X to distinguish from spatially varying densities in later sections.

The specific case of $\tilde{\Omega}_{\nu,{\rm m}}(a)$ in Equation (2) is calculated via

$$\tilde{\Omega}_{\nu,{\rm m}}(a) = \frac{7}{8} \sum_{i=1}^{N_\nu} \frac{4\sigma_B}{c\rho_{\rm crit}} \left(\frac{T_\nu^{\rm eff}}{a}\right)^4 \int_0^\infty dx \, x^2$$
$$\times \frac{\sqrt{x^2 + (\tilde{m}^i)^2}}{\exp(x) + 1}. \quad (6)$$

Here, σ_B is the Stefan–Boltzmann constant, c is the speed of massless particles, $\rho_{\rm crit}$ is the present critical density, and $T_\nu^{\rm eff}$ is the present effective temperature of the massive neutrinos. $T_\nu^{\rm eff}$ is related to the temperature of the CMB via $T_\nu^{\rm eff} = T_{\rm CMB} T_{\rm NCDM}$, where $T_{\rm NCDM}$ is a dimensionless factor ($\simeq 1$) used by, e.g.,

CLASS to set the ratio $\sum m_\nu / \Omega_{\nu,{\rm m}}$ to its experimentally measured value. Note that $T_{\rm NCDM}$ is used to modulate the effective temperature of massive neutrinos only; the temperature of relativistic neutrinos follows the usual relation in which $T_\nu = T_{\rm CMB}\left(\frac{4}{11}\right)^{1/3}$. Finally, $\tilde{m}^i$ is a per-species mass-dependent dimensionless constant, given by $\tilde{m}^i = m_\nu^i c^2 a/(k_B T_\nu^{\rm eff})$, where k_B is the Boltzmann constant.

Fitting models to cosmological observables requires predicting cosmological distances for a given model. We consider the comoving radial distance, which is calculated via a numerical integral as

$$\chi(a) = c \int_a^1 \frac{da'}{a'^2 H(a')}. \quad (7)$$

The comoving angular diameter distance is then computed in terms of the comoving radial distance:

$$r(\chi) = \begin{cases} K^{-1/2} \sin(K^{1/2}\chi) & K > 0 \\ \chi & K = 0, \\ |K|^{-1/2} \sinh(|K|^{1/2}\chi) & K < 0 \end{cases} \quad (8)$$

where $K \equiv \Omega_K H_0^2 c^{-2}$ is the curvature. The angular diameter distance is given by $d_A = a \, r(\chi(a))$, and the luminosity distance is $d_L = r(\chi(a))/a$, leading to the familiar relation $d_A = a^2 d_L$. The CCL suite also has the functionality to compute the distance modulus, defined as

$$\mu = 5 \log_{10}(d_L/{\rm pc}) - 5, \quad (9)$$

along with $a(\chi)$, the inverse function of $\chi(a)$.

2.2. Growth of Perturbations

In conjunction with the expansion rate, the growth history of the universe can allow us to distinguish between cosmological models. To compute the linear growth factor of matter perturbations, $D(a)$, CCL solves the following differential equation:

$$\frac{d}{da}\left(a^3 H(a) \frac{dD}{da}\right) = \frac{3}{2}\Omega_m(a) a H(a) D, \quad (10)$$

using a Runge–Kutta Cash–Karp algorithm. We define $g(a) \equiv D/a$ and adopt as initial conditions $g(a) = 1$ and $g'(a) = 0$ at sufficiently high redshift, during the matter-dominated era. CCL simultaneously computes the logarithmic growth rate $f(a)$, defined as

$$f(a) \equiv \frac{d \ln D}{d \ln a}. \quad (11)$$

CCL provides functions that return the growth normalized either to $D(a = 1) = 1$ or to $D(a \ll 1) \to a$. It employs an accelerated spline that is linearly spaced in the scale factor to interpolate the growth functions (for more details, see Section 3). The growth calculations cover flat and curved ΛCDM and wCDM cosmologies. However, it should be noted that the above treatment is ill defined in the presence of massive neutrinos, and attempts to compute the growth rate in cosmologies with massive neutrinos will produce an inconsistency between growth predictions and the matter power spectrum (Section 2.3), for example.

Finally, CCL allows for growth predictions with an alternative "modified gravity" cosmological model defined

by a regular curved wCDM background as well as a user-defined $\Delta f(a)$, such that the true growth rate in this model is given by

$$f(a) = f_0(a) + \Delta f(a), \tag{12}$$

where $f_0(a)$ is the growth rate in the background model. Note that this model is only consistently implemented with regard to the computation of the linear growth factor and growth rates and does not feed into other observables. This model, and the interpretation of the predictions given by CCL, should therefore be used with care.

2.3. Matter Power Spectrum

Theoretical predictions for cosmological observables such as galaxy clustering, gravitational lensing, and cluster mass functions rely on knowledge of the distribution of matter from small to large scales in the universe. To second order, the distribution of matter density fluctuations at a given wavenumber k and redshift is described by the matter power spectrum, $P(k, z)$, defined as

$$\langle \tilde{\delta}(\boldsymbol{k}, z)\tilde{\delta}(\boldsymbol{k}', z) \rangle = (2\pi)^3 P(k, z)\, \delta_D^3(\boldsymbol{k} + \boldsymbol{k}'), \tag{13}$$

where $\tilde{\delta}(\boldsymbol{k})$ is the Fourier component of the density field at a given wavenumber and δ_D^3 is the Dirac delta function. $P(k, z)$ has units of volume and a dimensionless analog is often defined as

$$\Delta^2(k, z) \equiv \frac{k^3}{2\pi^2} P(k, z). \tag{14}$$

At sufficiently large scales (small k), $P(k, z)$ can be obtained from solving linear perturbation-theory equations. In this case, $P(k, z)$ is referred to as the "linear" matter power spectrum. At small scales, where perturbation theory breaks down, other approaches based on numerical simulations are needed. In this more general case, $P(k, z)$ is referred to as the "nonlinear" matter power spectrum.

CCL implements several different methods for making predictions for the matter power spectrum. Two of those methods, the BBKS (Bardeen et al. 1986) and Eisenstein & Hu (1998) approximations, are only accurate to within a few percent and are implemented for validation purposes mainly. These approximations provide analytical expressions for the transfer function, $T(k)$, which is related to the matter power spectrum by $\Delta^2(k) \propto T^2(k)k^{3+n_s}$. There are two alternative ways to normalize the power spectrum. One option, which establishes a normalization at $z = 0$, is to provide a value for σ_8. The second option is to set the normalization at high redshift by giving a value for the amplitude of the primordial fluctuations, A_s. From the point of view of the CCL implementation, if the user provides σ_8, CCL also calculates the corresponding A_s for the specified cosmology.

The default CCL implementation uses the CLASS algorithm (Blas et al. 2011) to obtain predictions for $P(k, z)$. CLASS uses a Boltzmann solver to compute the linear power spectrum and also includes the halofit (Smith et al. 2003; Takahashi et al. 2012) fitting function for the nonlinear spectrum. In addition, CCL can also generate $P(k, z)$ predictions by emulating cosmological numerical simulations using the "Cosmic Emulator" developed by Lawrence et al. (2017).

We also provide a basic halo-model calculation of the nonlinear matter power spectrum which uses the included halo bias, halo mass function, and halo density profiles (see Sections 2.5–2.7). The power spectrum calculated via this method is not accurate enough for precision cosmology, with deviations as great as 50% compared to numerical simulations, but is pedagogically useful and we envisage expanding its functionalities to make it more realistic in the future.

None of the above methods account for the impact of baryonic physics on the distribution of matter, which is known to exceed the percent level at scales $k \gtrsim 1\,\mathrm{Mpc}^{-1}$ (van Daalen et al. 2011; Vogelsberger et al. 2014; Hellwing et al. 2016; Chisari et al. 2018; Springel et al. 2018) and can affect the extraction of cosmological parameters (Semboloni et al. 2011, 2013; Mohammed & Seljak 2014; Eifler et al. 2015; Mohammed & Gnedin 2017). To account for this effect, we incorporate in CCL an effective parameterization (Schneider & Teyssier 2015) of the redistribution of matter as a consequence of feedback from the active galactic nuclei and adiabatic cooling. We give an overview of each method to predict the matter power spectrum in what follows.

BBKS approximation. CCL implements the analytical BBKS approximation to the transfer function (Bardeen et al. 1986), given by

$$\begin{aligned} T(q) = & \frac{\ln[1 + 2.34q]}{2.34q} \\ & \times [1 + 3.89q + (16.2q)^2 + (5.47q)^3 + (6.71q)^4]^{-0.25}, \end{aligned} \tag{15}$$

where q is defined as follows (Sugiyama 1995)

$$q \equiv k/\{\Omega_m h^2 e^{-\Omega_b[1 + \sqrt{2h}/\Omega_m]}\mathrm{Mpc}^{-1}\}, \tag{16}$$

where k has units of Mpc^{-1}. The BBKS power spectrum option is primarily used as a precisely defined input for testing the numerical accuracy of CCL routines (as described in Section 3), and it is not recommended for other uses.

Eisenstein & Hu approximation. CCL also provides an approximation to the matter power spectrum as implemented by Eisenstein & Hu (1998; we refer the reader to this paper for a detailed discussion of the fitting formulae).[30]

CLASS. The default configuration of CCL adopts predictions for the linear and nonlinear matter power spectra from publicly available software (Blas et al. 2011). CLASS uses a Boltzmann solver to compute the linear power spectrum and makes predictions for the nonlinear power spectrum using the halofit prescription of Takahashi et al. (2012).

Cosmic emulator. An emulator method trained on numerical simulations (Lawrence et al. 2017) provides accurate predictions for the nonlinear matter power spectrum for $z \leqslant 2$ and in the wavenumber range $k = [10^{-3}, 5]\,\mathrm{Mpc}^{-1}$. The allowed range of cosmological parameters that can be passed

---

[30] Note that the implementation in CCL modifies Equation (5) of Eisenstein & Hu (1998) using $a^{-1} = 1 + z$ instead of the approximation $a^{-1} \sim z$. The difference in the resulting power spectra is negligible, but larger than 1 part in 10^4 for $k < 10\,h\mathrm{Mpc}^{-1}$.

to the emulator is as follows:[31]

$$
\begin{aligned}
0.12 &\leqslant \Omega_m h^2 \leqslant 0.155, \\
0.0215 &\leqslant \Omega_b h^2 \leqslant 0.0235, \\
0.7 &\leqslant \sigma_8 \leqslant 0.9, \\
0.55 &\leqslant h \leqslant 0.85, \\
0.85 &\leqslant n_s \leqslant 1.05, \\
-1.3 &\leqslant w_0 \leqslant -0.7, \\
-1.73 &\leqslant w_a \leqslant -0.7, \\
0.0 &\leqslant \Omega_{\nu,m} h^2 \leqslant 0.01.
\end{aligned}
\tag{17}
$$

In the case of the emulator, the effective number of relativistic neutrino species is set to $N_{\rm eff} = 3.04$ and $\Omega_\gamma = 0$. In Lawrence et al. (2017), the neutrino component of the power spectrum is not simulated, but either linearly evolved and added to the simulated power spectra at low redshift, or accounted for by a scale-dependent correction to the growth function. The typical accuracy of the emulator with respect to simulated power spectra is at the $<3\%$ level and depends on the cosmological model. More details on this method and its accuracy can be found in Upadhye et al. (2014), Castorina et al. (2015), and Heitmann et al. (2016).

Baryonic correction model (BCM). CCL incorporates the impact of baryons on the total matter power spectrum via the BCM of Schneider & Teyssier (2015). The main consequences of baryonic processes are to suppress the power spectrum at intermediate scales ($k \sim$ a few Mpc^{-1}), due to the heating and ejection of gas by active galactic nuclei feedback, and to enhance it at smaller scales, due to adiabatic cooling. To account for these effects, BCM uses an effective decomposition for the impact of gas ejection (G) and the enhancement of the small-scale profile due to star formation (S) to estimate the fractional effect of baryonic processes on the dark matter-only power spectrum ($P_{\rm DMO}$):

$$
P_{\rm BCM}(k, z) = P_{\rm DMO}(k, z) G(k|M_c, \eta_b, z) S(k|k_s).
\tag{18}
$$

Three effective parameters govern the contribution of baryonic processes to modifying the total matter power spectrum:

1. $\log_{10}[M_c/(M_\odot/h)]$: the mass of the clusters responsible for feedback, which regulates the amount of suppression of the matter power spectrum at intermediate scales;
2. η_b: a dimensionless parameter that determines the scale at which suppression peaks;
3. k_s [h Mpc^{-1}]: the wavenumber that determines the scale of the stellar distribution of matter in the center of halos.

If these parameters are not specified by the user, CCL assumes the default parameters of Schneider & Teyssier (2015), calibrated through different comparisons with observations and simulations in that work.

2.4. Two-point Correlators

The matter power spectrum is one of the necessary components to produce theoretical expectations for the two-point correlators of pairs of quantities (fields) that trace the matter density field in the universe. In this section, we will define these fields on the sky, such as galaxy positions or

galaxy shapes. These fields can be classified in terms of their spin s under rotations on the plane tangent to the sphere. In general a spin-s field is defined by two real-valued functions of the spherical coordinates $a_1(\hat{n})$ and $a_2(\hat{n})$ (e.g., γ_1 and γ_2 for weak lensing or the Stokes parameters Q and U in the case of polarized intensity), from which one can form the complex field $a = a_1 + ia_2$. For galaxy clustering, the galaxy density is a spin-0 field described by a scalar.

Spin-s quantities can be decomposed into their harmonic coefficients $_sa_{\ell m}$ through a spherical harmonic transform (Zaldarriaga & Seljak 1997; Reinecke 2011):

$$
_sa_{\ell m} = \int d\hat{n}\, a(\hat{n})_s Y^*_{\ell m}(\hat{n}), \quad a(\hat{n}) = \sum_{\ell m} {}_sa_{\ell m}\, {}_sY_{\ell m}(\hat{n}),
$$

where $_sY_{\ell m}$ are the spin-weighted spherical harmonics. The harmonic coefficients can then be associated with parity-even and parity-odd components (E-modes and B-modes respectively) as[32]

$$
\begin{aligned}
E_{\ell m} &= -\frac{1}{2}[\, {}_sa_{\ell m} + (-1)^s\, {}_{-s}a_{\ell m}] \\
iB_{\ell m} &= -\frac{1}{2}[\, {}_sa_{\ell m} - (-1)^s\, {}_{-s}a_{\ell m}],
\end{aligned}
\tag{19}
$$

where $_{-s}a_{\ell m}$ is defined as

$$
_{-s}a_{\ell m} = \int d\hat{n}\, a^*(\hat{n})_{-s} Y^*_{\ell m}(\hat{n}).
$$

In what follows, we will focus on scalar ($s = 0$) quantities such as the overdensity of source number counts or the CMB lensing convergence, and on spin-2 fields such as the lensing shear. We will also distinguish between *tracers* (fields observed on the sky, such as number counts in a redshift bin, shear, or CMB temperature fluctuations) and *contributions* to the total observed fluctuations of these tracers (such as the biased matter density term in number counts, redshift-space distortions (RSDs), magnification, etc.).

2.4.1. Angular Power Spectra

The angular power spectrum C_ℓ^{ab} between two tracers a and b is defined as

$$
\langle a_{\ell m} b^*_{\ell m} \rangle \equiv C^{ab}_\ell \delta_{\ell\ell'} \delta_{mm'},
\tag{20}
$$

where $a_{\ell m}$ and $b_{\ell m}$ can be either the E-mode or B-mode component of the corresponding field. In what follows, we will only work with fields for which the B-modes are exactly or nearly 0, and which we will take to be identically 0. Therefore, all equations refer to the *EE* power spectrum. In general, this power spectrum can be written as

$$
C_\ell^{ab} = 4\pi \int_0^\infty \frac{dk}{k}\, \mathcal{P}_\Phi(k) \Delta_\ell^a(k) \Delta_\ell^b(k),
\tag{21}
$$

where $\mathcal{P}_\Phi(k)$ is the dimensionless power spectrum of the primordial curvature perturbations, and Δ^a and Δ^b are the transfer functions corresponding to these tracers. Each transfer

---

[31] w_a and w_0 are constrained jointly to be $0.3 \leqslant (-w_0-w_a)^{1/4}$.

[32] We note that for spin-0 quantities, the minus sign preceding these equations is usually omitted, and we do so in what follows. Also, all scalar fields discussed here are real-valued, and therefore have zero B-modes.

function will receive contributions from different terms. CCL supports three types of tracers: number counts, galaxy-shape distortions, and CMB lensing convergence, with the following contributions:[33]

Number counts. The transfer function for number counts can be decomposed into three contributions: $\Delta^{\mathrm{NC}} = \Delta^{\mathrm{D}} + \Delta^{\mathrm{RSD}} + \Delta^{\mathrm{M}}$, where

1. Δ^{D} is the standard density term proportional to the matter density:

$$\Delta_\ell^{\mathrm{D}}(k) = \int dz\, p_z(z) b(z) T_\delta(k, z) j_\ell(k\chi(z)), \quad (22)$$

where $j_\ell(x)$ is the ℓth-order spherical Bessel function, T_δ is the matter overdensity transfer function, $b(z)$ is the linear clustering bias for this tracer, and $p_z(z)$ is the normalized distribution of sources in redshift. The fluctuations in the number density of sources in different redshift bins are therefore treated by CCL as different tracers. Note that CCL does not currently support nonlinear or scale-dependent bias, but future releases will do so under a number of schemes, including perturbative approaches as implemented in, e.g., McEwen et al. (2016).

It is also worth noting that the matter overdensity transfer function T_δ in Equation (22) is not the same as the transfer function used in Section 2.3. While $T(k)$ is defined as (Eisenstein & Hu 1998)

$$T(k) = \frac{\delta(k, z=0)}{\delta(k, z=\infty)} \frac{\delta(k=0, z=\infty)}{\delta(k=0, z=0)}, \quad (23)$$

all subscripted transfer functions T_X used here are defined as the ratio between the subscript quantity X and the primordial curvature perturbations:

$$X(\boldsymbol{k}, z) = T_X(k, z)\Phi(\boldsymbol{k}). \quad (24)$$

2. Δ^{RSD} is the linear contribution from RSDs:

$$\Delta_\ell^{\mathrm{RSD}}(k) = \int dz\, \frac{(1+z)p_z(z)}{H(z)} T_\theta(k, z) j_\ell''(k\chi(z)), \quad (25)$$

where $T_\theta(k, z)$ is the transfer function of θ, the divergence of the comoving velocity field, and j_ℓ'' is the second-order derivative of the spherical Bessel function, j_ℓ. Note that the RSD contribution to number counts is computed by CCL assuming a linear-theory relation between the matter overdensity and peculiar velocity fields, mediated by the scale-independent growth rate f (Equation (11)). While this should not be problematic for wide photometric redshift bins and standard cosmological models, users should exercise caution when interpreting results for narrow window functions or exotic cosmologies. Additionally, number count tracers with RSD in cosmologies with massive neutrinos are not currently supported.

3. Δ^{M} is the contribution from lensing magnification:

$$\Delta_\ell^{\mathrm{M}}(k) = -\ell(\ell+1) \int \frac{dz}{H(z)} W^{\mathrm{M}}(z)$$
$$\times\, T_{\phi+\psi}(k, z) j_\ell(k\chi(z)), \quad (26)$$

where $T_{\phi+\psi}$ is the transfer function for the Newtonian-gauge scalar metric perturbations, and W^{M} is the magnification window function:

$$W^{\mathrm{M}}(z) \equiv \int_z^\infty dz'\, p_z(z') \frac{2 - 5s(z')}{2} \frac{r(\chi' - \chi)}{r(\chi')r(\chi)}. \quad (27)$$

Here, $s(z)$ is the logarithmic derivative of the number of sources with a magnitude limit, and $r(\chi)$ is the angular comoving distance (see Equation (8)).

Note that CCL does not currently compute relativistic corrections to number counts other than magnification bias (Bonvin & Durrer 2011; Challinor & Lewis 2011). Although these will be included in the future, their contribution to the total fluctuation is largely subdominant (see Alonso et al. 2015 and the two references above), and therefore, it is safe to ignore them for our purposes.

Correlated galaxy shapes. The transfer function for correlated galaxy shapes (intrinsic and lensed) is decomposed into two terms: $\Delta^{\mathrm{SH}} = \Delta^{\mathrm{L}} + \Delta^{\mathrm{IA}}$, where

1. Δ^{L} is the standard lensing ("cosmic shear") contribution:

$$\Delta_\ell^{\mathrm{L}}(k) = -\frac{1}{2}\sqrt{\frac{(\ell+2)!}{(\ell-2)!}} \int \frac{dz}{H(z)} W^{\mathrm{L}}(z) T_{\phi+\psi}(k, z)$$
$$\times\, j_\ell(k\chi(z)), \quad (28)$$

where W^{L} is the lensing kernel, given by

$$W^L(z) \equiv \int_z^\infty dz' p_z(z') \frac{r(\chi' - \chi)}{r(\chi')r(\chi)}. \quad (29)$$

2. Δ^{IA} is the transfer function for intrinsic galaxy alignments. CCL supports the so-called "nonlinear alignment model" (NLA), in which the intrinsic galaxy inertia tensor is proportional the local tidal tensor (Catelan et al. 2001; Hirata & Seljak 2004; Hirata et al. 2007):

$$\Delta_\ell^{\mathrm{IA}}(k) = \sqrt{\frac{(\ell+2)!}{(\ell-2)!}} \int dz\, p_z(z) b_{\mathrm{IA}}(z) f_{\mathrm{IA}}(z)$$
$$\times\, T_\delta(k, z) \frac{j_\ell(k\chi(z))}{[k\chi(z)]^2}. \quad (30)$$

Here, b_{IA} is the so-called alignment bias, and f_{IA} is the fraction of aligned galaxies in the sample. Notice that $b_{\mathrm{IA}}(z)$ absorbs the typical normalization factors used in the literature for intrinsic alignment amplitude and redshift evolution. It is thus not to be confused with C_1 or A_{IA}, typical parameters adopted in works such as van Uitert et al. (2018), Joudaki et al. (2018), and Hildebrandt et al. (2017). In particular, the product $b_{\mathrm{IA}} f_{\mathrm{IA}}$ is equivalent to the quantity defined in Equation (8) of Hildebrandt et al. (2017). The NLA model has limitations in the modeling of small-scale correlations (Singh et al. 2015) and does not predict any B-mode contributions that can arise from nonlinearities at such scales. However, it is a commonly adopted approximation in the current literature and going beyond it is outside of the scope of this work, though future versions of LSST DESC software will provide alternative modeling options (Blazek et al. 2017).

CMB lensing. The transfer function for the lensing convergence, κ, of a given source plane at redshift z_* receives

---

[33] Note that we use units where the speed of light is $c = 1$ throughout.

only one contribution, given by

$$\Delta_\ell^\kappa(k) = -\frac{\ell(\ell+1)}{2} \int_0^{\chi_*} \frac{dz}{H(z)} \frac{r(\chi_* - \chi)}{r(\chi)r(\chi_*)} T_{\phi+\psi}(k, z), \quad (31)$$

where $\chi_* \equiv \chi(z_*)$.

It is worth noting that the equations above should be modified for nonflat cosmologies by replacing the spherical Bessel functions j_ℓ with their hyperspherical counterparts (Kamionkowski & Spergel 1994). These are currently not supported by CCL, and their impact is mostly relevant in low multipoles. The library also assumes a factorizable matter power spectrum at unequal times $P_\delta(k, z_1, z_2) = T_\delta(k, z_1)T_\delta(k, z_2)2\pi^2\mathcal{P}_\Phi(k)$. This approximation is widely used in the literature, but further work is needed to assess its impact on LSST observables (Kitching & Heavens 2017). Furthermore, CCL assumes a relation between transfer functions T_δ, T_θ, and $T_{\phi+\psi}$ that is strictly only valid in vanilla ΛCDM:[34]

$$T_\delta = -\frac{1+z}{H(z)f(z)}T_\theta = -\frac{k^2}{3H_0^2\Omega_m}\frac{T_{\phi+\psi}}{1+z}. \quad (32)$$

These approximations will be revisited in future versions of the library.

2.4.2. Correlation Functions

Fields are correlated in configuration space, and the corresponding correlators are called correlation functions. Let a and b be two fields with spins s_a and s_b. We start by defining $\tilde{a}(\hat{n}_1)$ and $\tilde{b}(\hat{n}_2)$ as the fields a and b rotated such that the x-axis of the tangential coordinate systems at directions $\hat{n}_1$ and $\hat{n}_2$ become aligned with the vector connecting both points. We can then define two correlation functions:

$$\xi_+^{ab}(\theta) \equiv \langle \tilde{a}(\hat{n}_1)\tilde{b}^*(\hat{n}_2)\rangle, \quad \xi_-^{ab}(\theta) \equiv \langle \tilde{a}(\hat{n}_1)\tilde{b}(\hat{n}_2)\rangle,$$

where $\hat{n}_1 \cdot \hat{n}_2 \equiv \cos\theta$.

$\xi_\pm$ can be related to the angular power spectra (Equation (20)) as

$$\xi_\pm^{ab} = \sum_\ell \frac{2\ell+1}{4\pi}(\pm 1)^{s_b} C_\ell^{ab\pm} d_{s_a,\pm s_b}^\ell(\theta), \quad (33)$$

where $d_{mm'}^\ell$ are the Wigner-d matrices (Ng & Liu 1999; Chon et al. 2004), and we have defined the power spectra

$$C_\ell^{ab\pm} \equiv (C_\ell^{a_E b_E} \pm C_\ell^{a_B b_B}) + i(C_\ell^{a_B b_E} \mp C_\ell^{a_E b_B}), \quad (34)$$

which reduces to the *EE* power spectrum when all *B*-modes are 0.

Note that, as scalar quantities are real, any correlation involving at least one spin-0 field only has one unique correlation function. In these cases, the Wigner-d matrices can also be expressed in terms of the associated Legendre polynomials P_ℓ^m, and therefore Equation (33) becomes

$$\xi^{ab}(\theta) = \sum_\ell \frac{2\ell+1}{4\pi} C_\ell^{ab} \sqrt{\frac{(\ell-s_a)!}{(\ell+s_a)!}} P_\ell^{s_a}(\cos\theta), \quad (35)$$

where we have assumed $s_b = 0$.

In the flat-sky approximation, we can take the small-scale limit $\ell \gg s_a, s_b$, and approximate

$$d_{s_a s_b}^\ell(\theta) \longrightarrow J_{s_a - s_b}(\ell\theta), \quad (36)$$

where $J_\alpha(x)$ is the Bessel function of order α. Equation (33) then becomes[35]

$$\xi_\pm^{ab}(\theta) = (\pm 1)^{s_b} \int \frac{d\ell\,\ell}{2\pi} C_\ell^{ab\pm} J_{s_a \mp s_b}(\ell\theta). \quad (37)$$

In summary, for spins 0 and 2, the three relevant cases for the cosmological observables supported by CCL are

1. $s_a = s_b = 0$ (e.g., galaxy–galaxy, galaxy–κ, and κ–κ:

$$\xi^{ab}(\theta) = \sum_\ell \frac{2\ell+1}{4\pi} C_\ell^{ab} P_\ell(\cos\theta) \quad \text{(full-sky)} \quad (38)$$

$$= \int_0^\infty \frac{d\ell\,\ell}{2\pi} C_\ell^{ab} J_0(\ell\theta) \quad \text{(flat-sky).} \quad (39)$$

2. $s_a = 2$, $s_b = 0$ (e.g., galaxy–shear, κ–shear):

$$\xi^{ab}(\theta) = \sum_\ell \frac{2\ell+1}{4\pi} C_\ell^{ab} d_{2,0}^\ell(\theta) \quad \text{(full-sky)} \quad (40)$$

$$= \int_0^\infty \frac{d\ell\,\ell}{2\pi} C_\ell^{ab} J_2(\ell\theta) \quad \text{(flat-sky),} \quad (41)$$

3. $s_a = s_b = 2$ (e.g., shear–shear):

$$\xi_\pm^{ab}(\theta) = \sum_\ell \frac{2\ell+1}{4\pi} C_\ell^{ab} d_{2,\pm 2}^\ell(\theta) \quad \text{(full-sky)} \quad (42)$$

$$= \int_0^\infty \frac{d\ell\,\ell}{2\pi} C_\ell^{ab} J_{2\mp 2}(\ell\theta) \quad \text{(flat-sky).} \quad (43)$$

In the following sections, we will specifically refer to the clustering correlation function in Equation (39) as ξ_{gg}.

2.4.3. Three-dimensional Spatial Correlation Function

In addition to the angular correlation functions, CCL can also compute the three-dimensional spatial correlation function, $\xi(r)$, from the following transformation of the matter power spectrum,

$$\xi(r) = \frac{1}{2\pi^2} \int_0^\infty dk\,k^2 P(k) \frac{\sin(kr)}{kr}. \quad (44)$$

In the future, CCL will be expanded to incorporate the calculation of the higher order multipoles needed to characterize the redshift-space three-dimensional correlation function in the presence of RSDs.

2.5. Halo Mass Function

Being able to calculate the halo abundance as a function of mass is a necessary step to constrain cosmology with probes such as galaxy clusters (Paranjape 2014). Modern cosmology makes extensive use of fitting functions in order to predict the evolution of halo abundances, which necessarily require derivation from cosmological simulations (Tinker et al. 2008, 2010; Angulo et al. 2012). We implement halo mass functions with parameters fit to these simulations. The

---

[34] Note that the transfer functions are defined here for the full nonlinear density field, as opposed to the more common linear transfer functions.

[35] See the weak-lensing review by Bartelmann & Schneider (2001) and Joachimi & Bridle (2010).

calculation of the halo mass function focuses around the spherical overdensity method of halo finding, in which a halo can be defined as a region of average density,

$$\bar{\rho}(r_\Delta) = \Delta_v \times \bar{\rho}_m, \tag{45}$$

equal to the overdensity parameter Δ_v times the mean background density of the universe at a given redshift, $\bar{\rho}_m(z)$, and with radius r_Δ. Within the literature, the choice of Δ_v can vary considerably, as observations focusing on the compact cores of halos often take much larger values of Δ_v than the fiducial definition in most halo-clustering studies, $\Delta_v = 200$. We note that an alternative definition exists that utilizes the critical density of the universe, ρ_{crit}, instead of the mean in Equation (45); this introduces a simple conversion factor between the two definitions that must be accounted for. CCL only accepts overdensity parameters with respect to the mean matter density, but we plan to allow for self-consistent handling of critical-density-based definitions in the future.

The halo mass function is defined as

$$\frac{dn}{dM} = f(\sigma) \frac{\bar{\rho}_m}{M} \frac{d\ln \sigma^{-1}}{dM}, \tag{46}$$

where n is the number density of halos of a given mass M associated with the rms variance of the matter density field, σ^2, at a given redshift and f is a fitting function.[36] CCL makes predictions for the mass function in logarithmic mass bins, $dn/d\log_{10}M$, where the input is the halo mass M and scale factor a.

The halo mass M is related to σ by first computing the radius R that would enclose a mass M in a homogeneous universe at $z = 0$:

$$M = \frac{H_0^2}{2G}R^3 \rightarrow \frac{M}{M_\odot} = 1.162 \times 10^{12} \Omega_m h^2 \left(\frac{R}{1\,\text{Mpc}}\right)^3. \tag{47}$$

The rms density contrast in spheres of radius R can then be computed as

$$\sigma_R^2 = \frac{1}{2\pi^2} \int dk\, k^2\, P_{lin}(k) \tilde{W}_R^2(k), \tag{48}$$

where $P_{lin}(k)$ is the linear matter power spectrum at $z = 0$ and $\tilde{W}(kR)$ is the Fourier transform of a spherical top-hat window function,

$$\tilde{W}_R(k) = \frac{3}{(kR)^3}[\sin(kR) - kR\cos(kR)]. \tag{49}$$

This is commonly related in terms of the mass inside of the Lagrangian scale of the halo, using the following transformation:

$$R = (3M/4\pi\bar{\rho}_m)^{1/3}. \tag{50}$$

As a consequence, one can also define σ_M as the rms variance of the density field smoothed on some scale M, analogously to Equation (48).

One commonly used halo mass function definition within the literature is the Tinker et al. (2010) fitting function. This fitting function has been developed using collisionless N-body simulation data, using halos identified by spherical overdensities.

This is an extension of the Tinker et al. (2008) halo mass function, which is also included within CCL as a comparative option. This fitting function assumes no change with respect to cosmological parameters except for changes in $\sigma_M(z)$.[37] Further, it includes a redshift scaling that is assumed to sharply end at a redshift of $z = 3$. This halo mass function is calibrated within the range of $10^{10.5}M_\odot\, h \leqslant M \leqslant 10^{15.5}M_\odot\, h$ at a redshift of $z = 0$.

For comparison purposes, we also have included the results of Angulo et al. (2012), which uses the Millennium XXL simulation in order to study galaxy cluster scaling relations. As part of their study, they calculated their own best-fit parameters for the Tinker et al. (2010) fitting function. While this additional halo mass function is available, it has not been extended to a broad range of overdensity parameter Δ_v, nor has it been extended beyond a redshift of $z = 0$.

The Tinker et al. (2008) fitting function uses the following parameterization:

$$f(\sigma) = A\left[\left(\frac{\sigma}{b}\right)^{-a} + 1\right]e^{-c/\sigma^2}, \tag{51}$$

where A, a, b, and c are fitting parameters that have additional redshift scaling. This basic form is modified for the Angulo et al. (2012) formulation. The resulting form is

$$f(\sigma) = A\left[\left(\frac{b}{\sigma} + 1\right)^{-a}\right]e^{-c/\sigma_M^2}, \tag{52}$$

where the only change is in the formulation of the second term. Note that the fitting parameters in the Angulo et al. (2012) formulation do not contain any redshift dependence, and its use is primarily for testing and benchmarking purposes.

The Tinker et al. (2010) model parameterizes the halo mass function in terms of the peak height, $\nu \equiv \delta_c/\sigma_M$, where $\delta_c = 1.686$ is the critical density for collapse (taken to be independent of cosmological model). The function is then re-expressed as

$$f(\nu) = \alpha[1 + (\beta\nu)^{-2\phi}]\nu^{2\eta}e^{-\gamma\nu^2/2}. \tag{53}$$

Tinker et al. (2008, 2010) quoted a 5% accuracy of their parametrized mass functions, compared to the simulations used to calibrate them. This result is consistent with the work of Watson et al. (2013), which also found a 5% level difference in comparison to the Tinker et al. (2008) fitting function. Further study will be required in the future in order to gain percent level accuracy in determining the halo mass function.

We note that these halo mass functions, while implemented to high numerical accuracy in CCL, carry their own uncertainties. It has not been significantly studied whether the halo mass function is universal with respect to changes in dark energy parameterization or, in general, to any other changes in cosmological parameters.

We also include the mass function from Sheth & Tormen (1999):

$$f(\nu) = A\left[1 + \frac{1}{(q\nu^2)^p}\right]e^{-q\nu^2/2}, \tag{54}$$

with $p = 0.3$, $q = 0.707$, and $A \simeq 0.21616$, where A is fixed such that the mass function is normalized.

---

[36] Not to be confused with the linear growth rate of structure defined in Equation (11).

[37] Tinker et al. (2008) stated that the difference in mass function between adopting *WMAP*1 and *WMAP*3 cosmologies was within 5%.

This mass function was fitted to halos measured in N-body simulations where halos were identified with a cosmology-dependent overdensity criterion from the spherical-collapse model ($\Delta_v \sim 300$ for $\Omega_m \sim 0.3$ ΛCDM; $\Delta_v \sim 178$ for $\Omega_m \sim 1$). For the cosmology dependence, we use the fitting formula of Bryan & Norman (1998),

$$\Delta_v(z) = \frac{1}{\Omega_m(z)}(18\pi^2 - 82x - 39x^2), \quad (55)$$

where $x = 1 - \Omega_m(z)$. In addition, in Sheth & Tormen (1999), the relation between M and ν was taken to include the cosmology dependence of $\delta_c(z)$, which derives from the spherical-collapse model. For this we use the fitting formula of Nakamura & Suto (1997):

$$\delta_c(z) = \frac{3(12\pi)^{2/3}}{20}\{1 + 0.012299 \log_{10}[\Omega_m(z)]\}. \quad (56)$$

2.6. Halo Bias

An important step in many interpretations of the halo model is to have a measure of the bias of dark matter halos, defined as the ratio of the halo power spectrum, $P_h(k)$, to the linear dark matter power spectrum,

$$b^2(k) = \frac{P_h(k)}{P_{lin}(k)}. \quad (57)$$

This is implemented as a stand-alone function in CCL and does not currently feed into predictions for galaxy or halo clustering described in Section 2.4.

As with measures of the halo mass function, high-accuracy cosmological constraints require the use of numerical simulations to develop fitting functions and emulators. Here, we define halos as in the above subsection. CCL implements the halo bias fitting function results from Tinker et al. (2010), though future improvements will likely require the use of emulator methods.

The Tinker et al. (2010) model parameterizes the halo bias in terms of the peak height and the critical density for collapse (similarly to Equation (53)) as

$$b(\nu) = 1 - A\frac{\nu^a}{\nu^a + \delta_c{}^a} + B\nu^b + C\nu^c. \quad (58)$$

Tinker et al. (2010) found a ~6% scatter when determining the halo bias due to differences in simulations alone. There is a remaining uncertainty on the physical accuracy of this model, as this parameterization does not consider any impact due to changes in the dark energy equation of state. As with the halo mass function, studies will be required to reach accuracy at the percent level for any cosmological predictions (e.g., Gao et al. 2005; Schulz & White 2006; Croton et al. 2007; Smith et al. 2007; Parfrey et al. 2011; Sunayama et al. 2016; Villarreal et al. 2017; Mao et al. 2018).

CCL can also make predictions for the halo bias from Sheth & Tormen (1999),

$$b(\nu) = 1 + \frac{1}{\delta_c(z)}\left[q\nu^2 - 1 + \frac{2p}{1 + (q\nu^2)^p}\right], \quad (59)$$

which can be derived using the peak-background split applied to Equation (54). Similar to that equation, $p = 0.3$, $q = 0.707$, and $\delta_c(z)$ is defined in Equation (56).

2.7. Halo Model

In this section, we review a basic halo-model computation (Peacock & Smith 2000; Seljak 2000; Cooray & Sheth 2002) of the cross-correlation between any two cosmological scalar fields. The calculation only requires knowledge of the halo profiles of the field in question. For example, in the case of the matter-density auto-spectrum, we need only know the halo density profiles. For the galaxy spectrum, we would require knowledge of the number of, and distribution of, galaxies as a function of halo mass (the so-called halo-occupation distribution). In this simple form, the halo model is approximate and makes the assumption that halos are linearly biased with respect to the linear matter field and also assumes that halos are spherical with properties that are determined solely by their mass. For the matter power spectrum, these assumptions mean that the matter power spectrum is only accurate to within a factor of 2 compared to that measured from numerical simulations (Mead et al. 2015). It is possible to go beyond these simplistic assumptions, and we direct the interested reader to Cooray & Sheth (2002), Smith et al. (2007), Giocoli et al. (2010), and Smith & Markovic (2011) for this.

The eventual aim for CCL is to have a halo model that can calculate the auto- and cross-spectra for any cosmological field combinations with parameters that can be taken either from numerical simulations or observational data. So far, we have only implemented the halo-model calculation of the density power spectrum, but we keep the notation as general as possible in the following.

Consider two three-dimensional cosmological scalar fields ρ_i and ρ_j, the cross-power spectrum at a given redshift can be written as a sum of a two- and a one-halo term. The two-halo term accounts for power that arises due to the distribution of halos with respect to one another, while the one-halo term accounts for power that arises due to the internal structure of individual halos. These terms are given by

$$P_{2H,ij}(k) = P_{lin}(k) \prod_{n=i,j}\left[\int_0^\infty b(M)\frac{dn}{dM}W_n(M, k)\, dM\right] \quad (60)$$

and

$$P_{1H,ij}(k) = \int_0^\infty \frac{dn}{dM}W_i(M, k)W_j(M, k)\, dM, \quad (61)$$

where M is the halo mass, dn/dM is the halo mass function defined in Equation (46), and $b(M)$ is the linear halo bias with respect to the linear matter density field, defined as the large-scale limit of Equation (57). The full halo-model power is then simply the sum

$$P_{HM,ij} = P_{2H,ij} + P_{1H,ij}. \quad (62)$$

Equations (60) and (61) contain the (spherical) Fourier transform of the halo profile, or the halo "window function":

$$W_i(M, k) = \int_0^\infty 4\pi r^2\frac{\sin(kr)}{kr}\rho_{H,i}(M, r)\, dr, \quad (63)$$

where $\rho_{H,i}(M, r)$ is the radial profile for the field i in a host halo of mass M. For example, if one is interested in calculating the matter power spectrum, then $\rho_{H,i}(M, r)$ would be the density contrast profile of a halo of mass M.

By default, in the halo-model calculation in CCL, we use the mass function and bias from Sheth & Tormen (1999). Note that the halo mass function and bias must satisfy the following

properties for the total power spectrum to have the correct large-scale limit, which is that the power should revert to the linear power spectrum

$$\frac{1}{\bar{\rho}_m} \int_0^\infty M \frac{dn}{dM} \, dM = 1, \tag{64}$$

and

$$\frac{1}{\bar{\rho}_m} \int_0^\infty M b(M) \frac{dn}{dM} \, dM = 1. \tag{65}$$

If one uses a mass function and bias pair that are related via the peak-background split formalism (Mo & White 1996; Sheth et al. 2001) then these conditions are automatically satisfied. In words, these equations enforce that all matter be associated with a halo. In the convention used in CCL, the units of $P_{\mathrm{HM},ij}(k)$ will be exactly the units of $\rho_i\rho_j/\mathrm{Mpc}^3$. The units of the W_i are those of the field ρ_i multiplied by volume.

For the matter power spectrum, we use the halo profiles of Navarro et al. (NFW; 1997):

$$\rho_H(M, r) \propto \frac{1}{r/r_s(1 + r/r_s)^2}. \tag{66}$$

The NFW profile is written in terms of a scale radius r_s. The constant of proportionality is fixed by the condition that the halo has total mass M integrated within the virial radius r_v. This radius is in turn set such that the halo has a fixed density Δ_v with respect to the mean. Hence, the following relation holds among mass, density, and radius:

$$M = 4\pi r_v^3 \Delta_v \bar{\rho}_m. \tag{67}$$

Finally, the scale radius is usually expressed in terms of the mass-dependent halo concentration parameter $c(M) = r_v/r_s$.

We use the mass–concentration relation from Duffy et al. (2008), appropriate for the full sample of halos defined using a virial Δ_v criterion,

$$c(M, z) = 7.85 \left(\frac{M}{M_p}\right)^{-0.081} (1 + z)^{-0.71}, \tag{68}$$

with $M_p = 2 \times 10^{12} \, h^{-1} \, M_\odot$. In order to be consistent one must use values of Δ_v and $c(M)$ that are consistent with the halo definition used for the halo mass function and bias. This consistency check is enforced by CCL, and we do not allow mixing of halo properties defined with different overdensity criteria.

2.8. Photometric Redshifts

Redshifts of LSST galaxies will be obtained via photometry. Therefore, performing any cosmological analysis that incorporates redshift information requires a model for the probability of measuring a photometric redshift z_{ph} for an object with true redshift z_t. In order to maintain agnosticism toward the optimal model, and hence to allow for the future inclusion of advancements from ongoing research, CCL allows the user to flexibly input a photometric redshift model. In addition, for ease of use, CCL provides the option of using a built-in function for a simple Gaussian photometric redshift probability distribution.

We define dN/dz as the true redshift distribution of a sample of galaxies, and dN^i/dz as the true redshift distribution of those galaxies that belong to the photometric redshift bin i. The photometric redshift model can then be used, for example, when computing dN^i/dz as given by

$$\frac{dN^i}{dz} = \frac{\frac{dN}{dz} \int_{z_i}^{z_{i+1}} dz' p(z, z')}{\int_{z_{\min}}^{z_{\max}} dz \frac{dN}{dz} \int_{z_i}^{z_{i+1}} dz' p(z, z')}, \tag{69}$$

where $p(z, z')$ is the photometric redshift probability distribution, and z_i and z_{i+1} are the photo-z edges of the bin in question. In the case of the simple Gaussian photometric redshift model for which native support is included in CCL, $p(z, z')$ is given by

$$p(z, z') = \frac{1}{\sqrt{2\pi}\,\sigma_z} \exp\left(-\frac{(z - z')^2}{2\sigma_z^2}\right), \tag{70}$$

where the user can set the value of σ_z, or indeed any arbitrary function may be provided for $p(z, z')$.

3. Implementation of High-accuracy Cosmological Functions

In this section, we note some of the assumptions and implementation details that are relevant when making accurate cosmological predictions. In general, we use the publicly available GSL library[38] to perform all of the integrations and interpolations. Most interpolations use the gsl_interp_akima method, and the power spectrum interpolation uses a bicubic spline provided by gsl_interp2d_bicubic. We work with double precision quantities throughout. The validation tests performed for CCL are described in detail in Section 4.

3.1. Background Functions and Growth of Perturbations

Cosmological predictions require making assumptions on the values of several physical constants, as defined in the previous sections. CCL adopts physical constant values from CODATA 2014 (Mohr et al. 2016) with the exception of the solar mass, which is not provided by this source and which we take from IAU 2015 (Mamajek et al. 2015).

We have performed a comparison of the physical constants used in CCL to those used in GSL and CLASS as well as published sources such as the NIST[39] Handbook and Particle Data Group Review of Particle Physics (Beringer et al. 2012). In general, we have found better than 10^{-4} agreement except for the gravitational constant and the value of the solar mass, where the discrepancies are nevertheless $<10^{-3}$. Notice that the value of these constants enters into the definition of the critical density (Equation (3)).

3.2. Matter Power Spectrum

For speed, the initialization of a cosmological model within CCL performs initial computations of the linear and nonlinear matter power spectra, which are then interpolated to be used whenever required. A bicubic spline is performed in two variables. The first one is the logarithmically spaced wavenumber. For the scale factor, we adopt a hybrid spacing scheme where this quantity is linearly spaced for $a > 0.1$ and logarithmically spaced otherwise. The goal of this hybrid

---

scheme is to allow sufficiently fine sampling at low redshift for LSST observables, while at the same time allowing for predictions for CMB lensing without significantly slowing down the computations, as would result from a linear spacing throughout. The spline interpolation causes some precision loss in the power spectra output (compared to, for example, direct outputs from CLASS or the Cosmic Emulator), which is quantified in Section 4.

We introduce a maximum value k (in units of Mpc^{-1}) up to which we evaluate the power spectra for interpolation; we call this parameter K_MAX_SPLINE. A separate K_MAX parameter sets the limit of evaluation of the matter power spectrum. The range between K_MAX_SPLINE $< k <$ K_MAX is evaluated by performing a second-order Taylor expansion in $\ln k$.

The Taylor expansion is implemented as follows: first, we compute the first and second derivatives of $\ln P(k, z)$ at $k_0 =$ K_MAX_SPLINE $- 2\Delta \ln k$ via finite difference derivatives using GSL. The fiducial choice for $\Delta \ln k$ is 10^{-2}. We then apply a second-order Taylor expansion to extrapolate the matter power spectrum to $k >$ K_MAX_SPLINE. The Taylor expansion gives

$$
\begin{aligned}
\ln P(k, z) \simeq {} & \ln P(k_0, z) + \frac{d \ln P}{d \ln k}(k_0, z)(\ln k - \ln k_0) \\
& + \frac{1}{2} \frac{d^2 \ln P}{d \ln k^2}(k_0, z)(\ln k - \ln k_0)^2.
\end{aligned}
\tag{71}
$$

We also extrapolate the power spectrum at small wavenumbers. In this case, we introduce the parameter K_MIN_SPLINE, the wavenumber below which the power spectra are obtained by a power-law extrapolation with index n_s:

$$
\begin{aligned}
\log & P(k < \text{K\_MIN\_SPLINE}, z) \\
& = \log P(\text{K\_MIN\_SPLINE}, z) \\
& + n_s(\log k - \log \text{K\_MIN\_SPLINE}).
\end{aligned}
\tag{72}
$$

Note that an additional parameter, K_MIN, sets the minimum k for integrations. This is set to K_MIN $= 5 \times 10^{-5}$ Mpc^{-1}.

The value adopted for K_MIN_SPLINE depends on the choice of power spectrum method and is not accessible by the user. For CLASS and the nonlinear power spectrum, we adopt K_MIN_S-PLINE, which coincides with the smallest wavenumber output by CLASS, K_MIN_SPLINE $= 7 \times 10^{-6}$ Mpc^{-1}. Hence, in practice, no extrapolation is occurring in this case. For BBKS, the power spectrum is computed analytically at all k; there is no extrapolation. For the Eisenstein & Hu (1998) implementation, the splines of the power spectrum span K_MIN $< k <$ K_MAX_S-PLINE, so there is only extrapolation at high k. For the nonlinear matter power spectrum from the emulator, K_MIN_SPLINE and K_MAX_SPLINE are set to fixed values that are determined from the range of validity of the emulator: K_MIN_SPLINE $= 10^{-3}$ Mpc^{-1} and K_MAX_SPLINE $= 5$ Mpc^{-1}.

3.3. Angular Power Spectra

Different numerical approaches have been implemented in the library in order to expedite the computation of angular power spectra. We describe these here. In all cases, to avoid calculating power spectra at all integer values of ℓ, by default CCL samples the power spectra at particular values of ℓ and interpolates between them to obtain the result at the ℓ values requested by the user. The sampling scheme is based on a combination of logarithmic samples at low ℓ and linear samples at high ℓ, although the particulars of the sampling scheme can

be configured by the user. A cubic-spline method is used to do the interpolation.

3.3.1. Limber Approximation

As shown in Section 2.4.1, computing each transfer function contributing to a given power spectrum involves a radial projection (i.e., an integral over redshift or z or χ), and thus, computing full power spectra consists of a triple integral for each ℓ. This can be computationally intensive, but can be significantly simplified in certain regimes by using the Limber approximation (Limber 1954; Afshordi et al. 2004), given by

$$
j_\ell(x) \simeq \sqrt{\frac{\pi}{2\ell + 1}} \, \delta\left(\ell + \frac{1}{2} - x\right).
\tag{73}
$$

This eliminates the integrals associated with each of the two transfer functions, accelerating the calculation significantly.

Thus, for each k and ℓ, we define a radial distance $\chi_\ell \equiv (\ell + 1/2)/k$, with the corresponding redshift z_ℓ. Substituting this in the expressions presented in Section 2.4.1, the power spectrum can be computed as a single integral:

$$
C_\ell^{ab} = \frac{2}{2\ell + 1} \int_0^\infty dk \, P_\delta(k, z_\ell) \tilde{\Delta}_\ell^a(k) \tilde{\Delta}_\ell^b(k),
\tag{74}
$$

where

$$
\tilde{\Delta}_\ell^{\mathrm{D}}(k) = p_z(z_\ell) b(z_\ell) H(z_\ell)
\tag{75}
$$

$$
\begin{aligned}
\tilde{\Delta}_\ell^{\mathrm{RSD}}(k) = {} & \frac{1 + 8\ell}{(2\ell + 1)^2} p_z(z_\ell) f(z_\ell) H(z_\ell) \\
& - \frac{4}{2\ell + 3} \sqrt{\frac{2\ell + 1}{2\ell + 3}} p_z(z_{\ell+1}) f(z_{\ell+1}) H(z_{\ell+1})
\end{aligned}
\tag{76}
$$

$$
\tilde{\Delta}_\ell^{\mathrm{M}}(k) = 3\Omega_{M,0} H_0^2 \frac{\ell(\ell + 1)}{k^2} \frac{(1 + z_\ell)}{\chi_\ell} W^{\mathrm{M}}(z_\ell)
\tag{77}
$$

$$
\tilde{\Delta}_\ell^{\mathrm{L}}(k) = \frac{3}{2} \Omega_{M,0} H_0^2 \sqrt{\frac{(\ell + 2)!}{(\ell - 2)!}} \frac{1}{k^2} \frac{1 + z_\ell}{\chi_\ell} W^{\mathrm{L}}(z_\ell)
\tag{78}
$$

$$
\tilde{\Delta}_\ell^{\mathrm{IA}}(k) = \sqrt{\frac{(\ell + 2)!}{(\ell - 2)!}} \frac{p_z(z_\ell) b_{\mathrm{IA}}(z_\ell) f_{\mathrm{red}}(z_\ell) H(z_\ell)}{(\ell + 1/2)^2}.
\tag{79}
$$

The Limber approximation works best for wide radial kernels and high ℓ. The integration in Equation (74) is performed via the Gauss–Kronrod quadrature, as are the integrals needed to estimate the lensing and magnification window functions (Equations (27) and (29)). The integration limits for Equation (74) are adapted to the shape of the window functions entering $\tilde{\Delta}^{a,b}$, with absolute limits given by the K_MIN and K_MAX parameters described in Section 3.2.

3.3.2. Beyond Limber: Angpow

The computation of the C_ℓ^{ab} without the Limber approximation is extremely costly in terms of computing time using this method, particularly if one wants to extensively explore a full cosmological parameter space. To overcome this issue, CCL provides fast non-Limber predictions by calling the Angpow software (Campagne et al. 2017a).

The angular power spectrum for two tracers C_ℓ^{ab} is computed in Angpow according to the following expression:

$$C_\ell^{ab} = \iint_0^\infty dz\,dz'\, p_{z_1}(z_1) p_{z_2}(z')$$
$$\times \int_0^\infty dk\, f_\ell(z, k) f_\ell(z', k). \qquad (80)$$

The auxiliary function $f_\ell(z, k)$ is defined as

$$f_\ell(z, k) \equiv \sqrt{\frac{2}{\pi}}\, k \sqrt{P_\delta(k, z)}\, \widetilde{\Delta}_\ell(z, k), \qquad (81)$$

with $\widetilde{\Delta}_\ell(z, k)$ the function describing the physical processes such as matter density fluctuations and RSDs as described, for instance, in Durrer (2008), Yoo et al. (2009), Yoo (2010), Challinor & Lewis (2011), and Bonvin & Durrer (2011).

The Angpow version delivered with CCL can only model galaxy clustering tracers (no gravitational lensing), and this without the magnification lensing term (Equation (26)). The incorporation of those transfer functions is left for future work, but in principle this is a straightforward extension of Angpow. For galaxy clustering tracers, we define $\widetilde{\Delta}_\ell(z, k)$ as

$$\widetilde{\Delta}_\ell(z, k) \equiv b(z) j_\ell(k\chi(z)) - f(z) j_\ell''(k\chi(z)) \qquad (82)$$

with $j_\ell(x)$ and $j_\ell''(x)$ the spherical Bessel function of order ℓ and its second derivative, and $f(z)$ the growth rate of the structure.

In Angpow, the inner integral in k is computed first. To conduct such computation where the integrand is a highly oscillating function, the 3C-algorithm described in details in Campagne et al. (2017a) is used. In brief, it relies on the projection of the oscillating $f_\ell(z, k)$ onto a Chebyshev series of order 2^N. The product of the two Chebyshev series is performed with a 2^{2N} Chebyshev series; then, the integral is computed using the Clenshaw–Curtis quadrature. Finally, the integrals over z are performed once again via an optimized Clenshaw–Curtis quadrature. All of the Chebyshev expansions and the Clenshaw–Curtis quadrature are performed via the discrete cosine transform of type I from the DCT-I fast transform of the FFTW library (Frigo & Johnson 2012).

As in the general case, the Limber approximation is valid at high ℓ values, the CCL user can define an ℓ threshold to switch from the non-Limber computation to the faster Limber approximation.

3.4. Correlation Functions

Computing the angular correlation functions essentially involves performing a linear transformation on the power spectra to go from harmonic to real space. The exact Equations (38)–(42) relating both quantities involve carrying out $N_\theta \times \ell_{max}$ operations, where $\ell_{max} \sim 10^4$–10^5 is the maximum multipole needed to achieve convergence and N_θ is the number of angular scales θ at which the angular correlation function needs to be computed. Thus, evaluating these expressions directly can become prohibitively slow and should be avoided except in regimes where other approximations are not valid. In particular, CCL only supports the brute-force evaluation of these equations for correlations involving at least one spin-0 field. The default method in CCL is to use the flat-sky approximation and evaluate the Hankel transforms (Equations (39), (41), and (43)).

CCL provides two methods to compute Hankel transforms:

Brute-force integration. CCL allows users to compute Hankel transforms by brute-force integration over the Bessel functions using an adaptive Gauss–Kronrod algorithm. The oscillating nature of these functions makes this method slow and not appropriate for likelihood sampling.

Thus, despite the higher precision of the brute-force integration approach, the preferred method for computing correlation functions is through the use of FFTlog (see below), and we support the brute-force method primarily for testing and validation.

FFTlog. The public code FFTlog[40] is able to compute fast Hankel transforms through the assumption that the kernels of these transforms are periodic functions in logarithmic space. The Hankel transform can then be solved using fast Fourier transforms at a much lower computational expense than brute-force integration (Hamilton 2000; Talman 2009). CCL incorporates a version of the FFTlog method with only minor modifications from the original. The only potential drawback of this method is the need to sample the kernels (i.e., the C_ℓ) on very small scales to ensure the convergence of the method. To do this, CCL extrapolates the power spectrum as a power law, assuming $C_\ell \propto \ell^\beta$, with a tilt β estimated from the logarithmic slope of the two last values of the C_ℓ provided as input. We have verified that this method agrees with the brute-force integration to well within cosmic-variance uncertainties.

We should also note that other approaches relating the correlation functions directly with the three-dimensional matter power spectrum (e.g., Campagne et al. 2017b) could be useful in accelerating this computation, and we will explore these in the future.

3.5. Halo Mass Function, Halo Bias, and Halo Model

The computation of the halo mass function requires obtaining the derivative of σ^{-1} with respect to mass, Equation (46). These derivatives are calculated utilizing a spline interpolation of $\sigma(M)$. These splines cover the range from 10^6 to $10^{17} M_\odot$. For each value of $\log(M)$ in our spline evaluation, we calculate the value of $\sigma(M)$ half a step in either direction. We use the difference compared to the mass spacing to calculate an approximate derivative, which is then used in the spline interpolation. The precision of this method was established for the halo mass function within the mass range explored by Tinker et al. (2010), and we give details of this in the next section. We note that the accuracy is reduced at the edges of these splines and exploring extreme mass ranges may require changes in the parameters to initialize these splines.

In order to accommodate a wide range of values of the overdensity parameter Δ_v, we have generated a spline interpolation between best-fit values as defined by Tinker et al. (2008, 2010). This covers a dynamic range from $\Delta_v = 200$ to 3200, with respect to the mean density. Within this range, we interpolate in the space of the fit parameter and $\log \Delta_v$ using the Akima interpolation built from piecewise third-order polynomials. We have chosen this rather than the fitting formulas utilized in Tinker et al. (2010) in order to assure a high-precision match to the Tinker halo mass function when choosing a value of Δ_v directly from the paper.

Calculations required to make predictions for the halo bias are analytical and are thus implemented in CCL. In the case of

---

[40] http://casa.colorado.edu/~ajsh/FFTLog/

the halo model, this phenomenological approach to modeling the matter power spectrum requires us to perform the integrations of the two-halo term (Equation (60)), the one-halo term (Equation (61)), and the window function (Equation (63)). For both Equations (60) and (61), we use `GSL_INTEG_GAUSS41` to perform the integration between the limits of 10^7 and 10^{17} solar masses with a relative error tolerance of 10^{-4}. Achieving the correct $k \rightarrow 0$ limit for the two-halo term, which should be exactly the linear power spectrum, is difficult numerically because of the large amount of mass contained in low-mass halos according to most popular mass functions. We deal with this for an arbitrary lower mass limit by enforcing the large-scale limiting behavior of the halo mass function (Equation (64)) by adding the mass missing from the integral as a delta function in mass at the lower limit in the two-halo integral in Equation (60). For NFW halos (Equation (66)), the integral required for the window function (Equation (63)) is analytical:

$$
\begin{aligned}
W_\delta(M, k) = \ & 4\pi r_s^3 \\
& \times \{ \sin(k r_s)[\mathrm{Si}(\{1 + c\} k r_s) - \mathrm{Si}(k r_s)] \\
& + \cos(k r_s)[\mathrm{Ci}(\{1 + c\} k r_s) - \mathrm{Ci}(k r_s)] \\
& - \frac{\sin(k r_v)}{(1 + c) k r_s} \},
\end{aligned}
\tag{83}
$$

where $\mathrm{Si}(x)$ and $\mathrm{Ci}(x)$ are the sine and cosine integral functions, and c is the concentration parameter defined in Section 2.7.

3.6. Massive Neutrinos

When initializing a cosmology with massive neutrinos within CCL, the user can provide either a single value for m_ν, corresponding to a sum of the masses of three neutrinos, or a set of three values, corresponding directly to the three masses. In the former case, one can also specify how the sum of masses should be split for calculations. The default behavior of CCL is to split the sum into three masses that are consistent with the normal neutrino mass hierarchy, but an inverted hierarchy or equal splitting can also be requested. (For a review of the neutrino mass hierarchies and relevant particle physics results, see, for example, Lesgourgues & Pastor 2012; Lattanzi & Gerbino 2017.)

For equal splitting, it is clearly trivial to compute the three neutrino masses. If splitting with respect to the normal or inverted hierarchy is desired, the mass calculation of the three masses is only marginally more complicated. The relevant known quantity, which has been determined via particle physics experiments, is the square of the difference of neutrino masses (up to a sign for one of the differences, hence the two possible hierarchies; see Lesgourgues & Pastor 2012; Lattanzi & Gerbino 2017). Because we know the square of the differences rather than the differences themselves, we must solve a set of quadratic equations for the neutrino masses. This is accomplished via a simple implementation of Newton's method, which converges to within machine precision in a few iterations.

Having then a set of three neutrino masses, we check which of the corresponding neutrino species is nonrelativistic today ($m_\nu > 0.00017$; Lesgourgues & Pastor 2012) and obtain the number of massive neutrinos in the cosmology. We use this, along with N_{eff}, to set the number of relativistic neutrino species, which is required in computing Ω_γ and $\Omega_{\nu,\mathrm{rel}}$. We must

be careful in doing so, as only for massive neutrinos do we modify the relationship between the temperature of the CMB and the neutrino temperature as described following Equation (6) above. The value of $N_{\nu,\mathrm{rel}}$ consistent with the user-provided N_{eff} is given by

$$
N_{\nu,\mathrm{rel}} = N_{\mathrm{eff}} - (T_{\mathrm{NCDM}})^4 \left(\frac{4}{11} \right)^{-\frac{4}{3}} N_{\nu,\mathrm{m}}.
\tag{84}
$$

In Equation (6) above, we specify how $\Omega_{\nu,\mathrm{m}}$ is computed for a given cosmology with massive neutrinos. Within this expression is a phase-space integral:

$$
\int_0^\infty dx \, x^2 \frac{\sqrt{x^2 + \tilde{m}^2}}{\exp(x) + 1}.
\tag{85}
$$

At high and low $\tilde{m}$, corresponding to high- and low-mass neutrinos, this integral need not be evaluated numerically. At high $\tilde{m}$, we set the integral equal to $5\zeta(3)\tilde{m}/(18\pi^4)$ (where ζ is the Riemann zeta function), while at low $\tilde{m}$, it goes to $7/8$. The $\tilde{m}$ values at which these approximations are taken can be set by the user. Outside of the regime in which these approximations are valid, the integral is computed numerically using GSL, splined, and stored such that for a single cosmology it must only be computed once.

It may sometimes be preferable or necessary to specify a cosmology in terms of $\Omega_{\nu,\mathrm{m}}$ instead of m_ν. To facilitate this, CCL includes a convenience function that returns m_ν given $\Omega_{\nu,\mathrm{m}}$. This is achieved via the relationship (see, e.g., Lesgourgues & Pastor 2012)

$$
\sum m_\nu = 93.14 \, \mathrm{eV} \times \Omega_{\nu,\mathrm{m}}
\tag{86}
$$

and then by splitting $\sum m_\nu$ into three neutrinos masses using the convention given by the user (the default being the normal mass hierarchy).

4. Validation

Our goal in building CCL was to ensure that all outputs are validated to a well-established high level of numerical accuracy. We described the core of our validation procedure in Section 1. Validation was achieved by performing different types of tests of CCL outputs. When possible, we established the accuracy of CCL against known analytic solutions. As there are few cases of observables and cosmologies for which there is such an analytic prediction, this is often not sufficient for our purposes. In one specific case (Section 4.2.4), we can compare the CCL outputs against numerical simulations, and there is a specific threshold of accuracy that needs to be achieved. Most commonly, we compare CCL outputs against one or multiple independent implementations obtained for the same cosmology. For such cases, we occasionally know the independent implementation to be more accurate. When this is not the case, we describe the differences between the implementations made by CCL and the independent benchmark code. Those independent implementations are provided and within the CCL repository together with our main library. For each feature, we define and quantify a numerical accuracy parameter, $\mathcal{A}$, in the following subsections, which describes the relative or absolute difference between the CCL prediction and the independent one.

Table 2
Summary of CCL Validation Tests and the Level of Agreement Achieved with Respect to the Benchmarks ($\mathcal{A}$)

Quantity	Equation/ Reference	Cosmologies	Range	Agreement with benchmarks, $\mathcal{A}$	Figure
Comoving radial distance, χ	(7)	CCL1–5,7–11	$0.01 \leqslant z \leqslant 1000$	5×10^{-7}	Figure 2
Growth factor, D	(10)	CCL1–5	$0.01 \leqslant z \leqslant 1000$	6×10^{-6}	Figure 2
$\sigma(M)$ (BBKS)	(48)	CCL1-3	$10^{10} \leqslant M/M_\odot \leqslant 10^{16}$	3×10^{-5}	Figure 8
$\log[\sigma^{-1}(M)]$ (BBKS)	(90)	CCL1	$10^{10} \leqslant M/M_\odot \leqslant 10^{16}$	10^{-3}	Figure 8
$\mathcal{H} \equiv \log[(M^2/\bar{\rho}_m)dn/dM]$	(91), Tinker et al. (2010)	CCL1	$10^{10} \leqslant M/M_\odot \leqslant 10^{16}$ and $z=0$	5×10^{-5}	Figure 8
$P(k)$ (BBKS)	(15)	CCL1-3	$10^{-3} \leqslant k/(h/\mathrm{Mpc}) \leqslant 10$ and $0 \leqslant z \leqslant 5$	10^{-5}	⋯
$P(k)$ (Eisenstein & Hu)	Eisenstein & Hu (1998)	CCL1	$10^{-3} \leqslant k/(h/\mathrm{Mpc}) \leqslant 10$ and $z=0$	10^{-5}	⋯
$P(k)$ (CLASS linear & HaloFit)[a]	Takahashi et al. (2012)	see Table 5	$10^{-3} \leqslant k/\mathrm{Mpc} \leqslant 20$ and $z = \{0, 2\}$	$\sim 10^{-3}$	Figures 3–6
$P(k)$ (CosmicEmu wCDM)[b]	Lawrence et al. (2017)	M1,M3,M M6,M8,M10	$10^{-3} \leqslant k/\mathrm{Mpc}^{-1} \leqslant 5$ and $z=0$	10^{-2}	Figure 7 (left panel)
$P(k)$ (CosmicEmu νCDM)[b]	Lawrence et al. (2017)	M38,M39,M40 M42	$10^{-3} \leqslant k/\mathrm{Mpc}^{-1} \leqslant 5$ and $z=0$	3×10^{-2}	Figure 7 (right panel)
$P(k)$ (Halo model)	Cooray & Sheth (2002)	CCL1, *WMAP7* *Planck* 2013	$10^{-4} \leqslant k/h\,\mathrm{Mpc}^{-1} \leqslant 10^2$ and $z = 0,1$	10^{-3}	Figure 10
$P(k)$ (baryonic)	(18), Schneider & Teyssier (2015)	⋯	$10^{-5} \leqslant k/h\,\mathrm{Mpc}^{-1} \leqslant 10$ and $z=0$	10^{-12}	⋯
C_ℓ clustering	(21), (22)	CCL6	$2 \leqslant \ell \leqslant 3000$	$0.1\sigma_\ell$	Figure 12
C_ℓ weak lensing	(21), (28)	CCL6	$2 \leqslant \ell \leqslant 3000$	$0.1\sigma_\ell$	Figure 12
C_ℓ gxy-gxy lensing	(21), (22), (28)	CCL6	$2 \leqslant \ell \leqslant 3000$	$0.1\sigma_\ell$	Figure 12
C_ℓ intrinsic alignments	(21), (30)	CCL6	$2 \leqslant \ell \leqslant 3000$	$0.1\sigma_\ell$	⋯
C_ℓ CMB lensing auto	(21), (31)	CCL6	$2 \leqslant \ell \leqslant 3000$	$0.1\sigma_l$	Figure 13
C_ℓ CMB lensing cross	(21), (22), (28), (31)	CCL6	$2 \leqslant \ell \leqslant 3000$	$0.1\sigma_\ell$	Figure 13
$\xi_\pm$, ξ_{gg}, ξ_{ggl}	(43), (41), (39)	CCL6	$0.01 < \theta/\deg < 5$	$0.5\sigma_{\mathrm{LSST}}$	Figures 14 and 15
3D correlation,[c] ξ	(44)	CCL1-3	$0.1 < r/\mathrm{Mpc} < 250$ and $0 \leqslant z \leqslant 5$	4×10^{-2}	Figures 16 and 17
C_ℓ clustering non-Limber	(21), (22), (25)	CCL1	$500 \leqslant \ell < 1000$	2×10^{-2}	⋯
C_ℓ clustering Angpow	(21), (22), (25)	CCL1	$2 \leqslant \ell < 1000$	3×10^{-3}	Figure 18 (right panel)

Notes. These tests can be reproduced by the user and are integrated into the CCL repository. The C_ℓ accuracy is set to 10% of the expected uncertainty, due to cosmic variance, σ_ℓ, given in Equation (96). In the case of intrinsic alignments, we validate the auto-spectra as well as cross-spectra with galaxy shear and positions. For this case, σ_ℓ includes the lensing contribution as well. Notice that the last row of the table compares the Angpow output for the clustering C_ℓ to an independent non-Limber implementation. The row immediately above demonstrates that the non-Limber method can also reproduce the limber case at high ℓ with sufficient accuracy compared to the expected cosmic variance. For the BCM case, we compared the fractional impact of baryons on the matter power spectrum by dividing the $P(k)$ prediction by the dark-matter-only case. Hence, the choice of cosmology becomes irrelevant in this case. Cosmologies are documented in Tables 3 and 4 for the "CCL" case, and in Lawrence et al. (2017) for the "M" cosmologies.
[a] Indicates that the accuracy was established against a known higher precision implementation.
[b] Indicates that a given level of accuracy was required in comparison to simulations.
[c] Indicates that at least one test was performed against an analytical solution.

The ultimate goal was to guarantee that any numerical uncertainty in the predictions for correlation functions are within a fraction of the expected statistical uncertainty for LSST. Moreover, we ensure that any prediction of the matter power spectrum, necessary for predicting cross-correlations between probes, has a well-established numerical accuracy. In this section, we document the numerical accuracy achieved for each observable and demonstrate that our overall goal has been achieved. We emphasize that the tests presented here pertain to numerical accuracy alone, while details of the physical accuracy of each model are provided in Section 2.

There are two cases where CCL is calling external codes to perform the computations. CLASS and the Cosmic Emulator, described in Section 2, are used by CCL in making power spectrum predictions. In doing so, and to improve on the speed of the code, power spectra from these codes are tabulated and interpolated. To ensure that this procedure does not introduce any significant deviations compared to the direct outputs of those codes, we compare CCL power spectra outputs to CLASS in Sections 4.2.2 and 4.2.3, and to the simulated power spectra used to calibrate the Cosmic Emulator in Section 4.2.4.

Table 2 summarizes all CCL validation tests discussed in this section. All plots presented in this section can be reproduced by means of a Python notebook available in the public repository. Accuracy checks can also be run automatically upon installation of the software. All independent scripts used to generate the predictions used to validate CCL are also released.[41]

In the following subsections, we also comment on potential discrepancies in the implementation of cosmological predictions between CCL and the benchmarks that could be responsible for the level of agreement achieved.

---

[41] A list of the scripts available can be found in the CCL wiki: https://github.com/LSSTDESC/CCL/wiki/Benchmarks.

Table 3
Cosmological Models with Massless Neutrinos Used in Testing CCL Against Independently Produced Benchmarks

	Cosmological Models with Massless Neutrinos								
Acronym	Model	Ω_m	Ω_b	Ω_Λ	h_0	σ_8	n_s	w_0	w_a
CCL1	flat ΛCDM	0.3	0.05	0.7	0.7	0.8	0.96	-1	0
CCL2	wCDM	0.3	0.05	0.7	0.7	0.8	0.96	-0.9	0
CCL3	wCDM	0.3	0.05	0.7	0.7	0.8	0.96	-0.9	0.1
CCL4	open wCDM	0.3	0.05	0.65	0.7	0.8	0.96	-0.9	0.1
CCL5	closed wCDM	0.3	0.05	0.75	0.7	0.8	0.96	-0.9	0.1
CCL6	flat ΛCDM	0.3	0	0.7	0.7	0.8	0.96	-1	0
WMAP7	flat ΛCDM	0.272	0.0455	0.728	0.704	0.810	0.967	-1	0
Planck 2013	flat ΛCDM	0.318	0.0490	0.682	0.671	0.834	0.962	-1	0

Table 4
Cosmological Models with Massive Neutrinos Used in Testing CCL Against Independently Produced Benchmarks

	Cosmological Models with Massive Neutrinos									
Acronym	Model	Ω_m	Ω_b	Ω_Λ	h_0	σ_8	n_s	w_0	w_a	$N_{\rm eff}$	m_ν (eV)
CCL7	flat ΛCDM, m_ν	0.3	0.05	0.7	0.7	0.8	0.96	-1	0	3.013	{0.04, 0, 0}
CCL8	wCDM, m_ν	0.3	0.05	0.7	0.7	0.8	0.96	-0.9	0	3.026	{0.05, 0.01, 0}
CCL9	wCDM, m_ν	0.3	0.05	0.7	0.7	0.8	0.96	-0.9	0.1	3.040	{0.03, 0.02, 0.04}
CCL10	open wCDM, m_ν	0.3	0.05	0.65	0.7	0.8	0.96	-0.9	0.1	3.013	{0.05, 0, 0}
CCL11	closed wCDM, m_ν	0.3	0.05	0.75	0.7	0.8	0.96	-0.9	0.1	3.026	{0.03, 0.02, 0}

Note. We calculate $N_{\rm eff}$ according to Equation (84), based on the number of massless and massive neutrino species.

4.1. Background Quantities and Growth of Perturbations

Comoving radial distances, the growth factor, and distance moduli were compared against independently produced benchmarks for redshifts between $z = 0.01$ and $z = 1000$. These comparisons were performed for the cosmologies listed in Table 3 and for the cosmologies with massive neutrinos listed in Table 4. (Notice that the growth function with massive neutrinos is not supported by CCL because it is scale dependent and therefore ill defined in our framework. Hence, no tests are provided for the growth function in those cosmologies.) The accuracy metric was defined as the fractional difference between the prediction made by CCL and by an independent implementation (labeled i), i.e., for the growth factor,

$$\mathcal{A} \equiv \frac{|D_{\rm CCL}(z) - D_i(z)|}{D_i(z)} \qquad (87)$$

and analogously defined for the comoving radial distance and distance moduli.

Figure 2 summarizes our results. The left panel shows the distance accuracy achieved for different cosmological models (curves of different thickness) as a function of redshift, which is always better than 5×10^{-7}. Distance comparisons are made against benchmarks produced with the CosmoMAD package[42] as well as the Python version for CLASS.[43] For speed, CCL relies on an intermediate instance where we adopt a specific grid for interpolating the comoving radial distance as a function of the scale factor for a given input cosmology. This instance is not there in CosmoMAD and can introduce additional uncertainty. CLASS similarly interpolates background quantities from a precomputed grid, but no efforts have been made to match the interpolation method or grid. Distance moduli in

CCL are also obtained from the interpolated comoving radial distance.

Similarly, the growth function is predicted with better than 6×10^{-6} accuracy in the right panel of Figure 2. The growth function is obtained by solving the differential Equation (10) by means of a Runge–Kutta Cash–Karp algorithm. CCL then adopts a specific grid for interpolating the growth function with the scale factor. CosmoMAD, used for benchmarking the growth function produced by CCL, implements a similar algorithm. Additional tests against independent codes (e.g., CosmoLike,[44] Krause et al. 2017; cosmosis,[45] Zuntz et al. 2015) for a wide range of wCDM models yielded agreement to 10^{-3}.

We validate the implementation of the modified growth function described in Equation (12) against an analytical prediction. In particular, we verify that, by setting $\Delta f(a) = k\,a$ for a constant k, the growth factor computed by CCL is compatible with the analytical solution $D(a) = D_0(a)\exp[k(a - 1)]$, where $D_0(a)$ is the solution for $\Delta f(a) = 0$, to better than one part in 10^5.

Additional independent distance benchmarks were obtained from astropy (Astropy Collaboration et al. 2013). We find that the agreement between CCL and astropy is only at the 10^{-3} level for cosmologies with massive neutrinos, in contrast to the much better agreement shown in the left panel of Figure 2, which relies on benchmarks obtained from CLASS. We believe that this is due to the fact that CCL uses the full phase-space integral in computing the massive neutrino density as defined in Equation (85), while astropy uses a fitting function that is itself only accurate at a 10^{-3} level. Hence, true accuracy is probably better than quoted and closer to the value reported in the first row of Table 2, as shown by Figure 2.
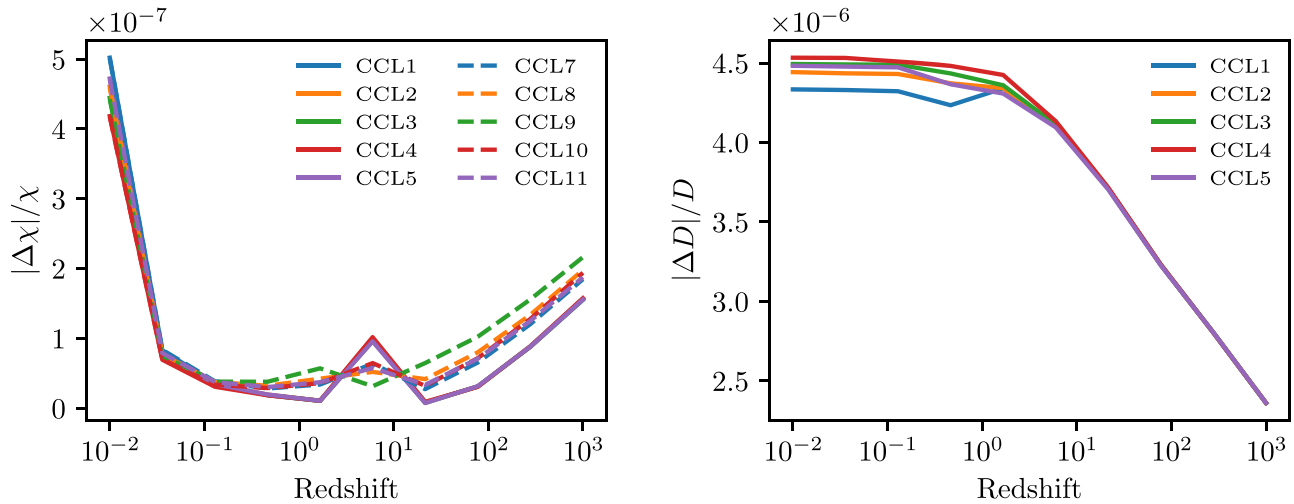

Figure 2. Accuracy achieved by CCL in the prediction of background quantities. Left panel: fractional difference between the predictions of the comoving radial distance by CCL and the benchmark for models CCL1–5 documented in Table 3 (solid lines) and models CCL7–11 with massive neutrinos documented in Table 4 (dashed lines). Right panel: fractional difference between the predictions of the growth factor by CCL and the benchmark for models CCL1–5. The growth factor in cosmologies with massive neutrinos is scale dependent and not supported by CCL.

4.2. Matter Power Spectra

4.2.1. Analytic Expressions

As discussed in Section 2.3, several power spectrum methods are implemented in CCL. Two of them, the BBKS (Bardeen et al. 1986) and the Eisenstein & Hu (1998) methods, are implemented for validation purposes only and feed into the tests for observables such as angular power spectra and correlation functions, as we will see in subsequent sections. These two implementations have been validated against independent implementations. The accuracy in this case was defined as the absolute fractional difference between the CCL and the independent predictions, i, at any given k and z:

$$\mathcal{A} \equiv \frac{|P_{\text{CCL}}(k, z) - P_i(k, z)|}{P_i(k, z)}. \tag{88}$$

For BBKS, this test was performed at $0 \leqslant z \leqslant 5$ in the wavenumber range $10^{-3} \leqslant k \leqslant 10 \ h\,\text{Mpc}^{-1}$ with 10 bins per decade, and yielded an accuracy level of 10^{-5}.[46] For the Eisenstein & Hu (1998) matter power spectrum, we obtained similar accuracy at $z = 0$ for the same wavenumbers. The cosmologies for which the tests were implemented are specified in Table 2.

For both BBKS and the Eisenstein & Hu (1998) matter power spectra, the comparisons with CCL were performed using CosmoMAD. As in CCL, CosmoMAD implements analytical functions to produce these predictions and then creates an interpolation of the result with logarithmic wavenumber. The level of agreement between CCL and the benchmarks is sensitive to the choice of interpolation scheme and resolution for the power spectrum in k and redshift.

The BCM implementation for the impact of baryons on the matter power spectrum, described in Section 2.3 is also analytical. Following Equation (88), we found it to be accurate to 10^{-12}. In this case, we expect no sources of discrepancy between the independent implementation and CCL other than

the numerical precision of the variables involved in the computation.

4.2.2. Validation of Interpolation Schemes

In its default configuration, CCL adopts the halofit (Takahashi et al. 2012) implementation by interpolating CLASS . power spectra outputs to model the matter power spectrum. The computation of the power spectrum from CLASS can be significantly sped up by interpolating the matter power spectra in the range K_MIN_SPLINE $< k <$ K_MAX_SPLINE and extrapolating beyond it, as described in Section 3. In this section, we describe the loss of accuracy due to this method. The tests presented are performed in a flat ΛCDM cosmology similar to CCL1, but with a normalization of the power spectrum set by $A_s = 2.1 \times 10^{-9}$ rather than σ_8.

The accuracy of this approximation is shown in Figure 3 for redshifts $z = 0$, $z = 3$, and $z = 20$. We compare the nonlinear matter power spectrum at these redshifts, computed with the previously described approximation, to the matter power spectrum obtained by setting the power spectrum splines to high-accuracy values. We find that for typical values of $\Delta \ln k = 10^{-2}$ and K_MAX_SPLINE $= 50\,\text{Mpc}^{-1}$, $\ln P$ has converged to an accuracy that surpasses the expected impact of baryonic effects on the matter power spectrum at $k > 10\,\text{Mpc}^{-1}$. (For an estimate of the impact of baryons on the total matter power spectrum, see Schneider & Teyssier 2015.)

With the implementation described above, the power spectrum splines are initialized up to K_MAX_SPLINE. This is also true for the linear matter power spectrum, which is used within CCL in particular to obtain σ_8 (see Equation (48)). We have tested how this procedure affects the convergence of the linear matter power spectrum. We compare the fiducial CCL output to the case where we increase the precision of all spline parameters by an order of magnitude (i.e., we use 10 times larger sampling rates in k and a, and extend the interpolation ranges in k by one decade on either end). The result is shown in Figure 3. For some applications that use the linear power spectrum, the user might need to increase the value of K_MAX_SPLINE, but overall, the impact of the fiducial interpolation parameters is negligible for most applications.

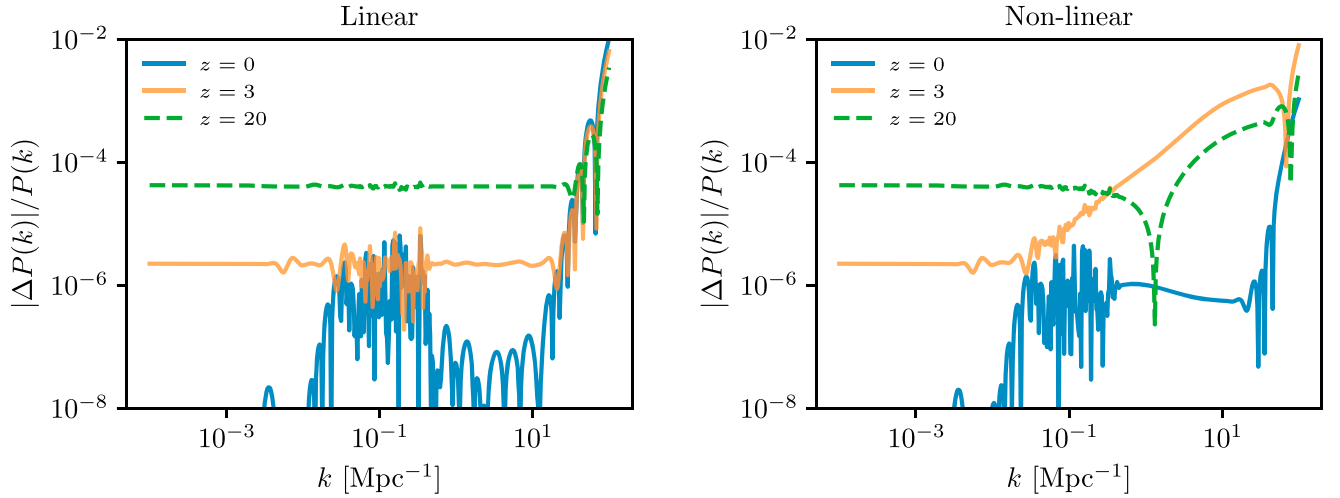[46] We noticed that there are two typographical errors for the BBKS transfer function in "Modern Cosmology" (Dodelson 2004) compared to the original BBKS paper. The quadratic term should be $(16.1q)^2$ and the cubic term should be $(5.46q)^3$. The BBKS equation is correct in Peacock (1999). Using the wrong equation can give differences in the results above the 10^{-4} level.

Figure 3. Relative error compared to power spectra produced with high values of the power spectrum splines, $P_{\rm fid}$, produced by splining the matter power spectrum up to `K_MAX_SPLINE = 50 Mpc`$^{-1}$ and extrapolating beyond this value with a second-order Taylor expansion of the natural logarithm of the matter power spectrum. The left panel shows the relative errors for the linear matter power spectrum at $z = 0$, $z = 3$, and $z = 20$. The right panel shows the results for the nonlinear matter power spectrum at the same redshifts. While the relative error increases substantially at high k, we note that it is still well below the uncertainty from baryonic physics at these scales, which is $\sim 10\%$ at $k = 1$ Mpc^{-1} (Schneider & Teyssier 2015).
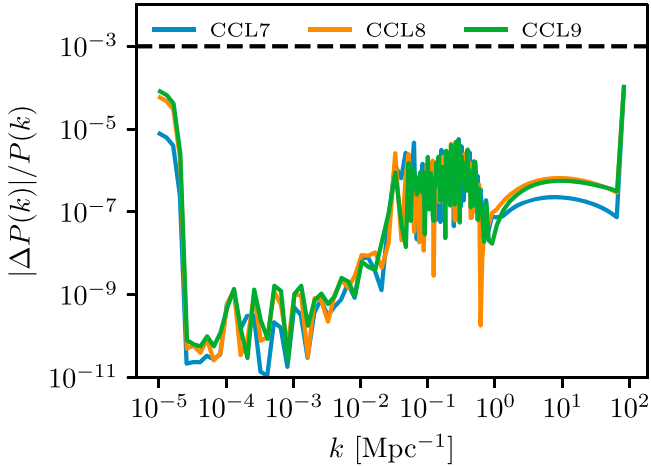
Figure 4. Fractional difference between the nonlinear matter power spectrum as computed directly via `CLASS` with that computed using `CLASS` via `CCL` in cosmologies CCL7, CCL8, and CCL9 with massive neutrinos.

In addition to the above tests in ΛCDM cosmologies without massive neutrinos, we have checked the impact of using splines (at intermediate k) and extrapolation (at low and high k) in cosmologies CCL7, CCL8, and CCL9, defined in Table 4. We compare the linear and nonlinear matter power spectra as computed directly via `CLASS` to that computed using `CLASS` via `CCL`. We find that for k between `K_MIN` and `K_MIN_SPLINE`, the two power spectra agree to better than 10^{-4} in all models. For k between `K_MAX_SPLINE` and `K_MAX`, agreement is better than 10^{-3}, which is sufficient given the significant physical uncertainties introduced at these small scales by effects such as galaxy formation (van Daalen et al. 2011). The fractional difference between the two nonlinear power spectra is shown in Figure 4.

4.2.3. Generalized Validation of the Power Spectrum over ΛCDM Parameter Space

While concentrating on individual points in cosmological parameter space allows us to perform detailed validation tests,

Table 5
Ranges of ΛCDM Parameters Used for the Generalized `CCL` Validation Tests of the Matter Power Spectrum

Parameter	Range
h	[0.55, 0.8]
Ω_c	[0.15, 0.35]
Ω_b	[0.018, 0.052]
A_s	[1.5, 2.5] $\times 10^{-9}$
n_s	[0.94, 0.98]

as above, it is important for `CCL` to also be validated across a wide range of cosmological parameter values, e.g., to ensure the validity for MCMC analyses. In this section, we present a set of validation tests for the `CCL` linear and nonlinear matter power spectrum functions that spans a broad range of ΛCDM parameters.

Covering a full range of all five ΛCDM parameters on a regular grid would be prohibitively expensive, so an alternative method for fairly (but more sparsely) sampling the parameter space is needed. We use Latin Hypercube Sampling to determine a tractably sized set of sample points. This splits the parameter space into a grid with N bins per dimension. The sample points are then chosen by going through each dimension in turn and choosing a bin at random without replacement, so that a given bin in each dimension is only ever chosen once. This is repeated until all bins in each dimension contain a single sample (or until a maximum number of sample points has been reached). This has the effect of covering the space uniformly but sparsely, with only N sample points chosen from the N^5 available positions on the grid. The exact location of the sample within each bin can be chosen from a uniform distribution within that bin, but for simplicity, we put each sample at the bin center. We use $N = 100$ sample points per dimension, with the ranges for each parameter given in Table 5. These ranges were chosen to be significantly wider than those allowed by current observational constraints, to ensure that the full parameter range expected to be accessed by MCMC analyses is covered. For the purposes of this exercise,
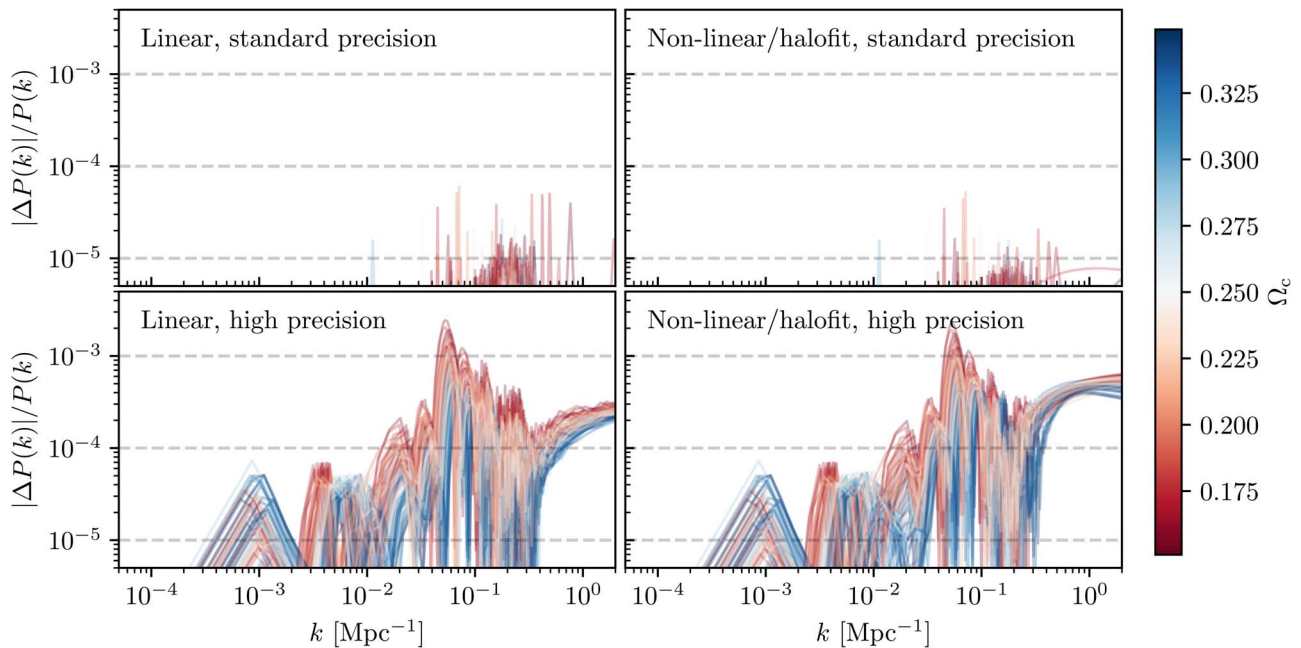
Figure 5. Absolute fractional difference between the matter power spectra at $z = 0$ calculated using CLASS via CCL, and CLASS directly, for a range of cosmological parameter values, and different CLASS precision settings (standard vs. high-precision) and power spectrum types (linear vs. halofit). The lines are colored according to the value of Ω_c for each set of cosmological parameters (see Table 5 for the ranges of other parameters).

we allow only massless neutrinos ($N_{\rm eff} = 3.046$) and set $T_{\rm CMB}$ to the same value in CCL and CLASS.

For each set of parameters, we then calculate the linear and nonlinear (halofit) power spectra using CCL for a range of redshifts. A corresponding set of reference power spectra is then produced using CLASS directly, i.e., using a regular installation of CLASS (v2.6.3). We run this with either default precision settings ("standard precision"), or settings intended to produce high-precision CMB results ("high precision"), taken from the pk_ref.pre precision file that is bundled with CLASS.

Figure 5 shows the fractional difference between the CCL and CLASS matter power power spectra at $z = 0$ for 100 sample points over the parameter space, with each line colored according to the value of Ω_c for that sample. Results for different power spectrum types (linear versus halofit) and CLASS precision settings are shown for comparison.

As shown in the top two panels of Figure 5, CCL reproduces the standard CLASS results well across a broad range of parameter values, always remaining well within a fractional precision of 10^{-4}. This demonstrates the robustness of our choice of spline parameters to different cosmological parameter values.

The lower panels in Figure 5 show the fractional deviation between CCL (which always uses the "standard" CLASS precision) and CLASS with high-precision settings. These deviations are more significant, especially around the wavenumbers where the baryon acoustic oscillation feature is most prominent. The precision is still generally better than 10^{-3}, however, and is only worse than that for the very lowest values of Ω_c.

Figure 6 shows the same comparison, but now for $z = 2$. The precision on the linear matter power spectrum is almost an order of magnitude worse than that at $z = 0$ for the standard precision settings (but still always better than 10^{-4}), and only slightly worse than that at $z = 0$ for the high-precision settings.

The picture is slightly different for the halofit power spectrum, however, where moderate deviations are seen for the standard precision settings in models with small values of Ω_c. This appears to be caused by a setting inside CLASS that switches off halofit corrections when a redshift- and cosmology-dependent threshold is reached, and can be mitigated by increasing the value of the P_k_max_1/Mpc parameter (which is already set to a relatively high value of 50 in CCL by default). Larger values of Ω_c produce only slightly worse precision than at $z = 0$, and the high-precision halofit results are also relatively unchanged.

These results show that the CLASS-based CCL power spectrum calculations are robust across a broad range of cosmological parameters, especially for the linear power spectrum, but that some caution must be taken when using the halofit power spectrum in MCMC studies that involve higher redshifts, for example.[47]

4.2.4. Validation of the Cosmic Emulator Implementation

The matter power spectrum emulation procedure from Lawrence et al. (2017) has an intrinsic accuracy compared to the simulated results used for its construction. It effectively provides a fitting scheme that allows interpolation between the simulation results. As a consequence, the method itself has some limitations in how well it can reproduce the simulation results. CCL takes the emulator predictions and interpolates between the wavenumber and scale-factor notes in the emulator output. To validate the final power spectra coming out of CCL, we compared them directly to the simulated spectra from Lawrence et al. (2017) for a subset of the cosmologies adopted in that work. In this section, we quantify the accuracy of the

---

[47] Note that the K_MAX_SPLINE setting in the ccl_params.ini file can be used to change the value of P_k_max_1/Mpc used for the halofit calculation, so this issue can be avoided at the expense of an increase in runtime.
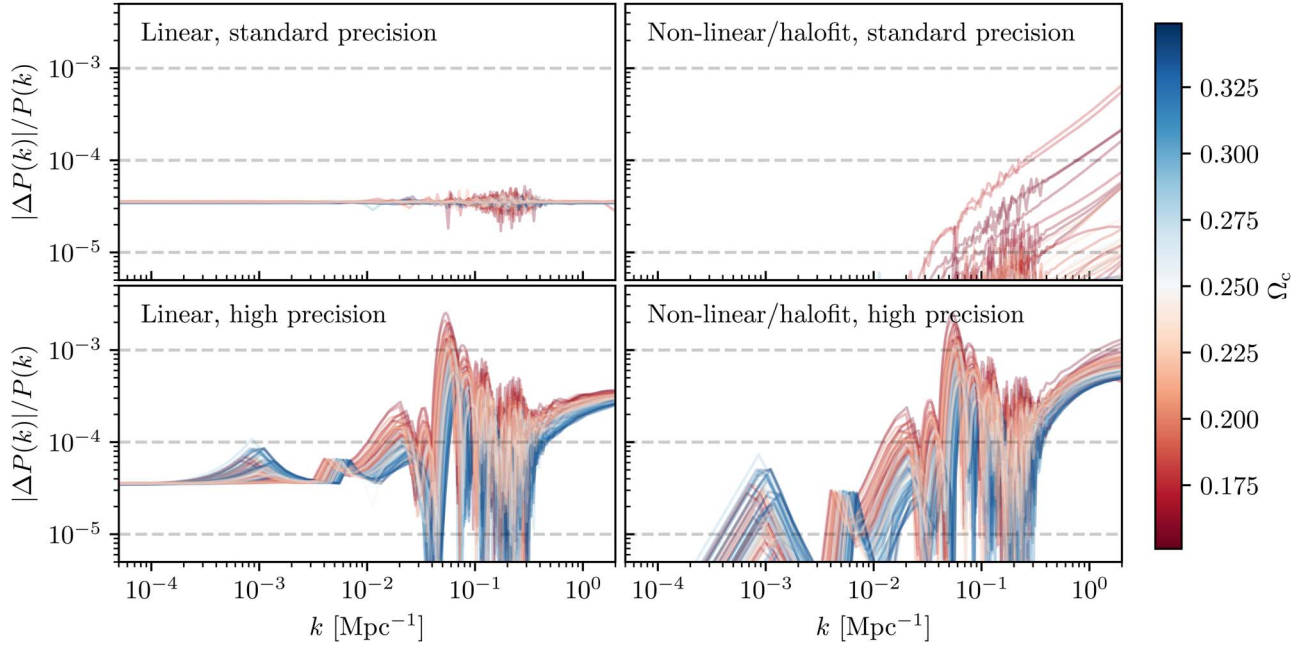
Figure 6. Absolute fractional difference between CCL and CLASS matter power spectra, as plotted in Figure 5, but now at $z = 2$.
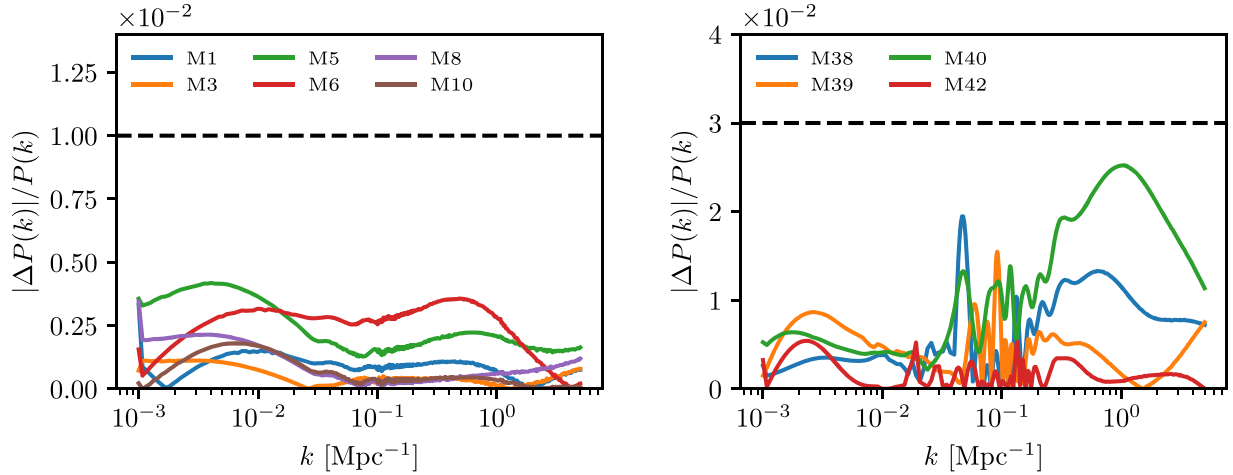

Figure 7. Absolute fractional accuracy in the matter power spectra, Equation (89), obtained by calling the Cosmic Emulator from CCL and the smoothed simulated spectra from Lawrence et al. (2017). The left panel shows the results for cosmologies without neutrinos; the right panel, results for cosmologies with neutrinos. The dashed line in both panels represents our target accuracy, based on the claimed accuracy of the emulator by Lawrence et al. (2017).

CCL predictions by estimating

$$\mathcal{A} \equiv \frac{|P_{\mathrm{CCL}}(k, z) - P_{\mathrm{L17}}(k, z)|}{P_{\mathrm{L17}}(k, z)}, \qquad (89)$$

where the label L17 refers to the smoothed simulated power spectra from Lawrence et al. (2017). Notice that the emulator is intrinsically accurate to 1% for cosmologies without massive neutrinos, and to 3% for cosmologies with massive neutrinos. In other words, replacing $P_{\mathrm{CCL}}(k, z)$ in Equation (89) by the direct emulator output would yield an $\mathcal{A}$ of 0.01 and 0.03 for the two different families of cosmologies. In the validation test presented in this section, we focus on ensuring that CCL does not deviate from that overall level of accuracy.

Our results are shown in Figure 7. For cosmologies without neutrinos, we required the matter power spectrum at $z = 0$ to be within 1% of the smoothed simulated power spectrum from Lawrence et al. (2017; see their Figure 6). Similarly, we

required 3% accuracy for cosmologies with neutrinos (their Figure 5). The cosmologies that were tested are the ones listed in Table 3, whose parameter values are specified in Lawrence et al. (2017). In both cases, we find that the CCL implementation falls below the target accuracy for the full range of scales tested. This is not surprising, as CCL directly incorporates the publicly available emulator prediction code.[48] The essential difference in the implementation is that the predictions of the public code for the matter power spectrum are interpolated in wavenumber and scale factor as we described in Section 3.2.

4.3. Halo Bias and Halo Mass Function

The accuracy of the halo mass function calculation was checked against benchmarks produced by CosmoMAD for power spectra obtained using the BBKS approximation, which

---

[48] https://github.com/lanl/CosmicEmu
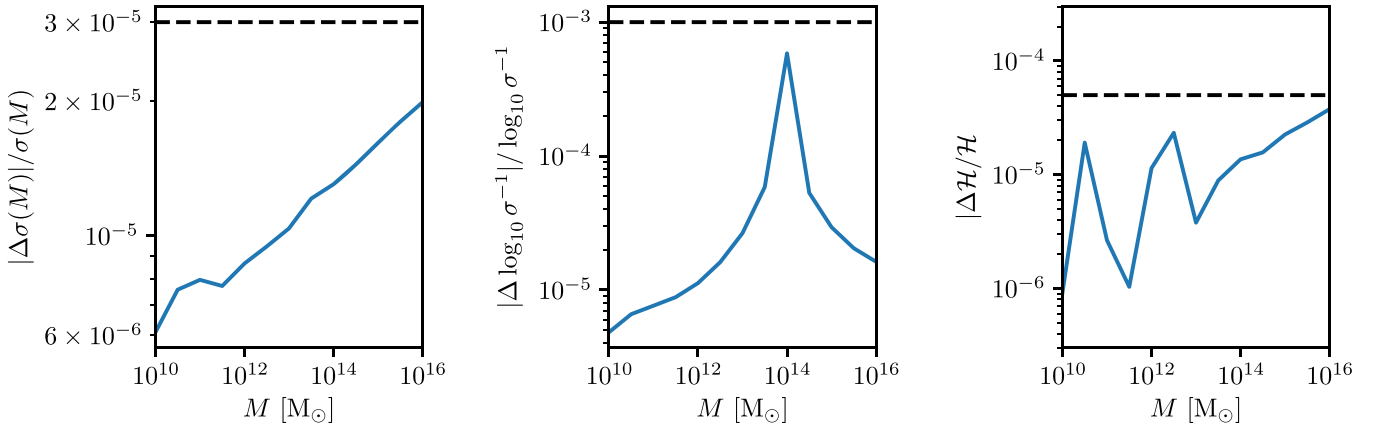
Figure 8. Three different numerical tests of the halo mass function calculation. In each panel, the blue line is the fractional error in the function, while the black dashed line represents our error tolerance. The first panel demonstrates the robust calculation of $\sigma(M)$. The second panel demonstrates a numerical quirk in our spline treatment that is currently not addressed, but does reduce the numerical accuracy in returning the log inverse of $\sigma(M)$. We note that this does not significantly impact the error in the halo mass function in the final panel.

allows us to isolate the numerical inaccuracies associated with the mass function calculation from those arising from the power spectrum calculation. For the halo mass function, we compare the value of σ,

$$\tilde{\sigma} \equiv \log[\sigma^{-1}(M)], \qquad (90)$$

and the value of the halo mass function in the form used in Tinker et al. (2008),

$$\mathcal{H} \equiv \log[(M^2/\bar{\rho}_m)\,dn/dM]. \qquad (91)$$

We define three new accuracy metrics:

$$\mathcal{A}_{\mathrm{hmf1}} \equiv \frac{|\sigma_{\mathrm{CCL}} - \sigma_i|}{\sigma_i}, \qquad (92)$$

$$\mathcal{A}_{\mathrm{hmf2}} \equiv \frac{|\tilde{\sigma}_{\mathrm{CCL}} - \tilde{\sigma}_i|}{\tilde{\sigma}_i}, \qquad (93)$$

$$\mathcal{A}_{\mathrm{hmf3}} \equiv \frac{|\mathcal{H}_{\mathrm{CCL}} - \mathcal{H}_i|}{\mathcal{H}_i}. \qquad (94)$$

Note that for $\sigma(M)$, it is important to set the desired precision level correctly for the numerical integrator. As the integral yields $\sigma^2(M)$, this becomes the relevant concern for numerical accuracy.

For $\mathcal{A}_{\mathrm{hmf1}}$ and $\mathcal{A}_{\mathrm{hmf3}}$, we achieve accuracies of 3×10^{-5} and 5×10^{-5}, respectively. For $\mathcal{A}_{\mathrm{hmf2}}$, the accuracy degrades to a value of 10^{-3}. These accuracy levels are acceptable, as it is significantly better than the physical accuracy of current halo mass function models. This is demonstrated in Figure 8, where this calculation has been run for a single cosmology using the Tinker et al. (2010) halo mass function.[49] While there is a degradation in accuracy due to our spline treatment of the log inverse of $\sigma(M)$, we note that it does not significantly degrade our halo mass function determination. While improvement on this remains a task for the future, the halo mass function varies between fitting functions significantly more than this remaining error. As of this time, we do not have independent implementations for the halo bias function, though it should be noted that this calculation does not involve any additional functions beyond $\sigma(M)$ and should not exceed a 10^{-4} tolerance level. Some deviation may exist between CCL and other

---

[49] A single cosmology is used for this analysis as the Tinker fitting parameters do not vary with cosmology.
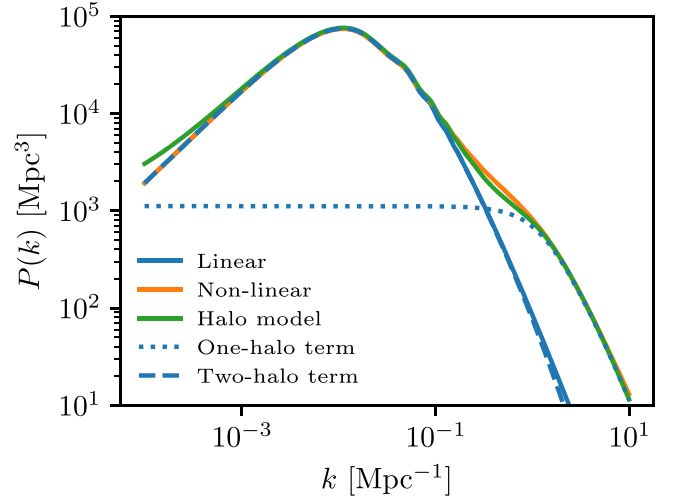
Figure 9. Matter power spectrum computed according to linear theory, `halofit`, and the CCL halo model for the CCL1 cosmology. The halo model two- and one-halo terms are also shown; their sum is the total halo model prediction. `halofit` is accurate compared to N-body simulations at the $\simeq$5% level for the scales shown. The halo-model prediction deviates from `halofit` at the $\simeq$30% level in the transition region when both the two- and one-halo terms are important ($k \simeq 0.5$ Mpc^{-1}) but shows better agreement at smaller scales.

implementations, due to our choice of spline interpolation between Tinker et al. (2010) fitting parameters as a function of Δ_{v}; we use an Akima interpolation between those provided in Tinker et al. (2010) for the halo mass function, and this may lead to mild numerical change. This approach is motivated by the fact that the difference in parameters at $\Delta_{\mathrm{v}} = 200$ between the fitting formula result and the tabulated best-fit parameters, leading to a greater than 10^{-4} error from our calculated benchmarks in the halo mass function. As the tabulated version is in common use in the literature, having higher accuracy for the tabulated points was prioritized.

4.4. Halo Model

In Figure 9, we show the power spectrum computed by the CCL halo model compared to that from `halofit` and to the linear matter spectrum for the CCL1 cosmology from Table 3 at $z = 0$. The halo-model predictions show the correct general trend for the
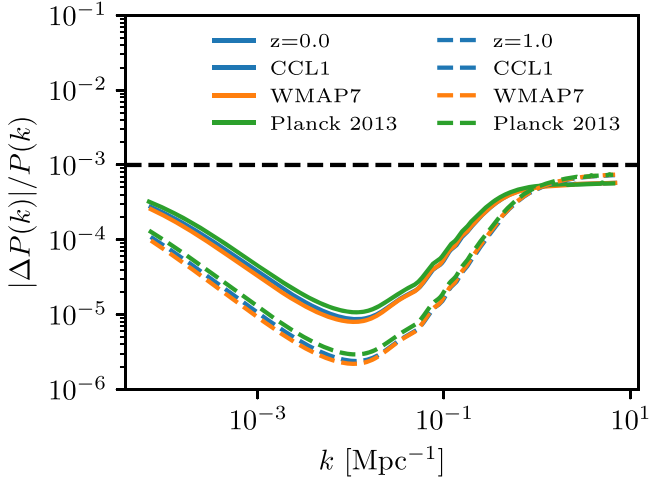
Figure 10. Relative accuracy of the halo-model power spectrum calculation compared to our benchmarks. We achieve a precision of 10^{-3} for the range of scales shown. Solid lines show $z = 0$ while dashed lines show $z = 1$. Different colors show different cosmological models (CCL1, *WMAP7*, *Planck* 2013).
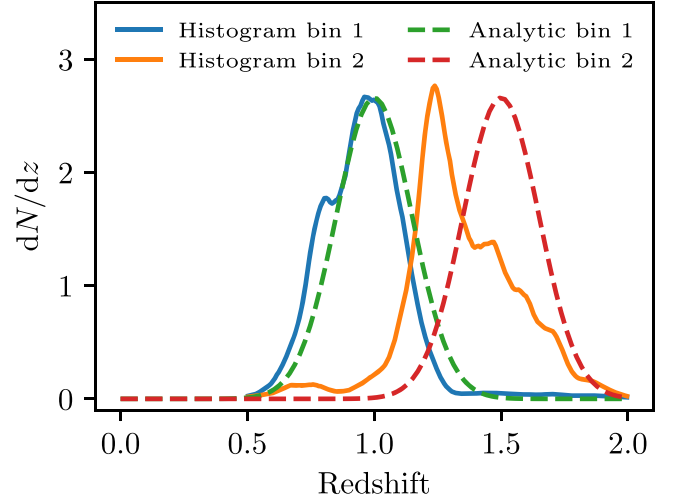

Figure 11. Redshift distributions used for validating the computation of angular power spectra and correlation functions.

nonlinear power spectrum but differ in details. Compared to simulations, they are only accurate at the ∼30% level.

In Figure 10, we show the accuracy of the halo-model power spectrum compared to our independently produced benchmark. The benchmark was generated using a standalone `Python` script that uses the CCL power spectrum as input, but includes independent implementations of the halo profiles and concentration–mass relations. The script produced predictions for the one-halo and two-halo contributions to the power spectrum, solving the corresponding mass integrals using the trapezium rule and `scipy`'s `quad` method. We define an accuracy criterion $\mathcal{A}$ as the ratio of the power from `CCL` compared to that from the independent code released with the `CCL` repository. With this definition, we achieve an accuracy of 10^{-3} across scales from $10^{-4}\,\mathrm{Mpc}^{-1} < k < 10\,\mathrm{Mpc}^{-1}$ for three different cosmological models (CCL1, *WMAP7*, *Planck* 2013) at both $z = 0$ and $z = 1$. The mass range for the halo-model integrations is identical for the benchmark and the `CCL` implementation, as are the mass function, halo bias, and halo profiles. Therefore, we suspect that the residual differences are due to the differing integration schemes between the benchmark and `CCL`. The benchmark shown here was produced using the nonadaptive trapezium rule, so this level of difference is not surprising.

4.5. Two-point Statistics

Validation tests for two-point statistics relied on the BBKS linear matter power spectrum. This choice of method was intended to remove any potential discrepancies between the `CCL` implementation and the independent one with regard to the matter power spectrum. By using BBKS, we are relying on predictions that we know to be fast and which we have already validated to known numerical accuracy (Section 4.2.1).

We thus used the BBKS linear matter power spectrum to compare two-point statistics for two redshift bins, resulting in four tomographic combinations, labeled 1–1, 1–2, 2–1, and 2–2. The validation tests were performed for two kinds of redshift distributions: analytic and binned ones. The goal of defining these two sets was to capture any numerical deviation produced by the interpolation of the binned distribution. We adopted the following analytic redshift distributions: a Gaussian with $\sigma = 0.15$, centered at $z_1 = 1$; and another

Gaussian with the same dispersion but centered at $z_2 = 1.5$. In the case of the binned distributions, we adopted the two redshift distribution histograms shown in Figure 11.

For both types of distributions, we computed the following quantities:

1. Number counts angular power spectra: density term only (no magnification, RSD, etc.) with nonevolving linear bias $b(z) = 1$ in the range $2 \leqslant \ell \leqslant 3000$.
2. Lensing E-mode angular power spectra: leading-order term only (no magnification), on the same scales.
3. The cross-power spectrum between galaxy positions and galaxy shear (galaxy–galaxy lensing), on the same scales.
4. Intrinsic alignment E-mode angular power spectra, cross-spectra with galaxy shear and galaxy positions, on the same scales, with $b_{\mathrm{IA}}(z)$ set to correspond to the commonly used parameterization of alignment amplitude (e.g., Joudaki et al. 2018) with $A_{\mathrm{IA}} = 1$ and $f_{\mathrm{IA}}(z) = 1$.
5. The cross-power spectrum between number counts and CMB lensing, on the same scales.
6. The cross-power spectrum between galaxy weak lensing and CMB weak lensing, on the same scales.
7. Number count angular correlation functions in the range $0°\!.01 < \theta < 8°$, using five bins per decade, and
8. Lensing shear angular correlation functions (ξ_+, ξ_-), similarly to above.
9. The cross-correlation between both quantities (galaxy–galaxy lensing), as above.
10. The full shape–shape and shape–position observables for both angular power spectra and correlation functions, where the intrinsic alignment contributions to the observables are included.

Notice that the RSD and magnification predictions are not currently validated. We do not include real-space (correlation function) benchmarks involving CMB lensing, because they are functionally the same as number counts (i.e., a spin-0 quantity). The angular power spectrum and correlation function benchmarks for the full "3 × 2pt" calculation of galaxy clustering and weak-lensing observables were created internally by `CosmoLSS`[50] and other independent codes.

---

50 https://github.com/sjoudaki/cosmolss

For C_ℓ computations, we define as our accuracy metric the absolute value of the difference between CCL and an independent realization, i, as a fraction of the cosmic-variance-limit uncertainties:

$$\mathcal{A} = \left| \frac{C_\ell^{\mathrm{CCL}} - C_\ell^{(i)}}{\sigma_\ell} \right|. \qquad (95)$$

For the power spectrum C_ℓ^{ab} between two fields a and b, the cosmic-variance errors are given by

$$\sigma_\ell^2 = \frac{C_\ell^{aa} C_\ell^{bb} + (C_\ell^{ab})^2}{2\ell + 1}. \qquad (96)$$

Our accuracy requirement, for all auto- and cross-correlations with analytic and binned redshift distributions, is $\mathcal{A} < 0.1$ (i.e., differences must be smaller than one-tenth of the cosmic-variance errors). Notice that Equation (96) assumes a full-sky survey. As a consequence, our requirement is conservative compared to a survey covering 40% of the sky, as expected for LSST, where the uncertainty from cosmic variance would be ∼60% larger.

The results for the auto- and cross-correlations between number counts and weak lensing are shown in Figure 12, while those involving CMB lensing are shown in Figure 13. In addition, we have verified that the intrinsic alignment auto-spectra and cross-spectra with shear and galaxy positions satisfy our accuracy requirement (intrinsic–intrinsic, shear–intrinsic, galaxy–intrinsic, and the full observables, i.e., II, GI, gI, GG+II+GI, gG+gI). In this case, the denominator in Equation (95) includes the lensing contribution as well.

The differences between the CCL results and the benchmarks are mostly due to the integration and interpolation methods. CosmoLSS is written in Fortran (compared to CCL, which is written in C) independently of any other existing cosmic shear, galaxy–galaxy lensing, and galaxy clustering code. It obtains the expansion history and comoving distance with redshift from CAMB (in general, CAMB also provides the matter power spectrum, which is, however, taken to be the same BBKS $P(k)$ as CCL here). It uses cubic-spline interpolation for the redshift distributions, it performs the integral of the lensing kernel using Romberg's method, and for the outer integral, to obtain the angular power spectra, it uses the trapezoidal rule with 370 logarithmically spaced bins over the full redshift range (it also allows the user to choose Romberg's method for this outer integral). The integral from angular power spectra to correlation functions is performed through a direct summation over all integer multipoles in the range $1 < \ell < 59,000$ (other choices of ℓ_{max} and integration methods have been explored and found to yield consistent results). For purposes of benchmarking CCL, while the impact is negligible, the angular power spectra are not interpolated in this process but directly computed at each of the multipoles.

The independent code that produces additional galaxy–galaxy lensing benchmarks is written in Python and has a number of differences with respect to CCL. It is not only redshift distributions that are interpolated prior to the computation of the angular power spectra, but also lensing kernels. Integration over redshift is performed using the quad routine in Python with a prespecified relative accuracy threshold of 10^{-7}. The angular power spectrum is then
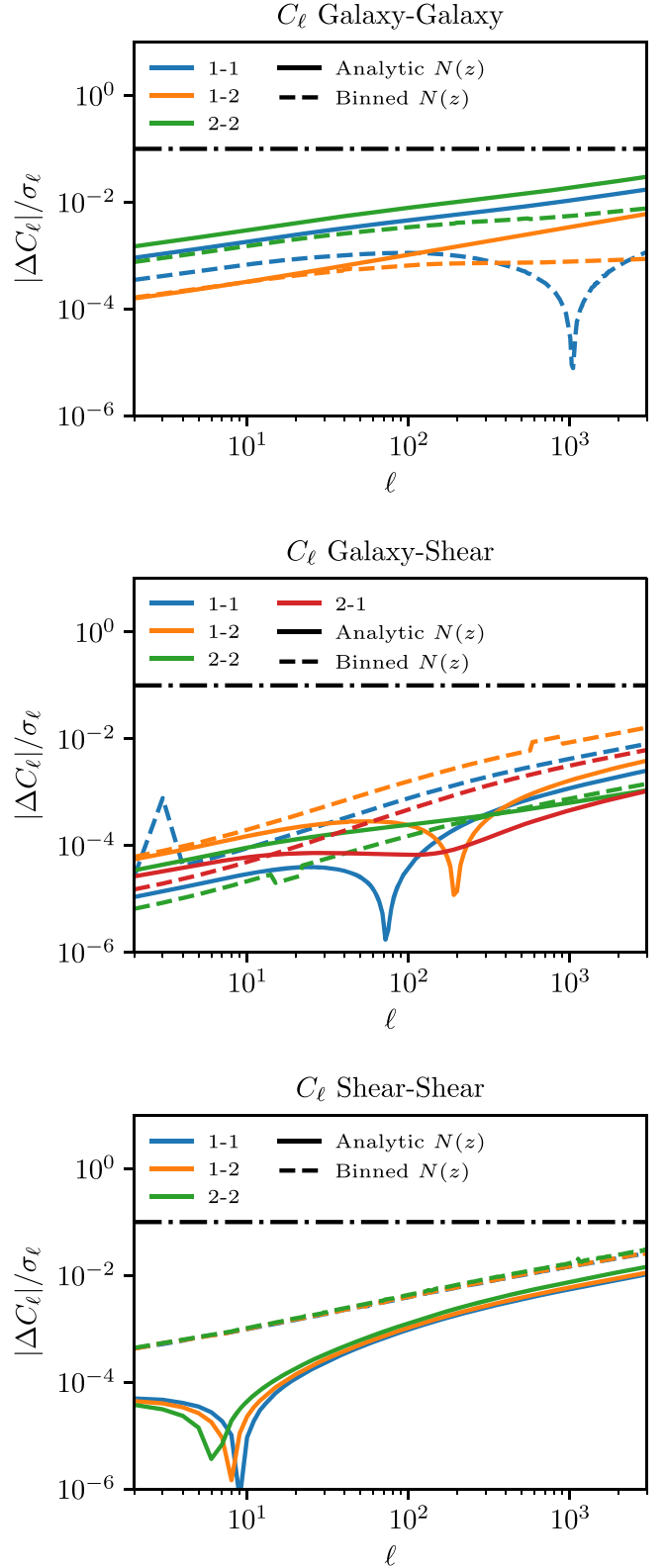
Figure 12. Tests of the angular power spectrum accuracy. The black dotted–dashed line indicates the target numerical accuracy of $0.1\sigma_\ell$. Top: benchmark comparisons for power spectra between number counts in pairs of redshift bins. Results are shown for analytic (solid) and binned (dashed) redshift distributions, for the bin pairs 1–1 (blue), 1–2 (orange), and 2–2 (green). Middle: same as the top panel for cross-correlations between number counts and weak lensing, this time including the tomographic bin combination 2–1 (red). Bottom: same as the top panel, but for the weak-lensing power spectra.
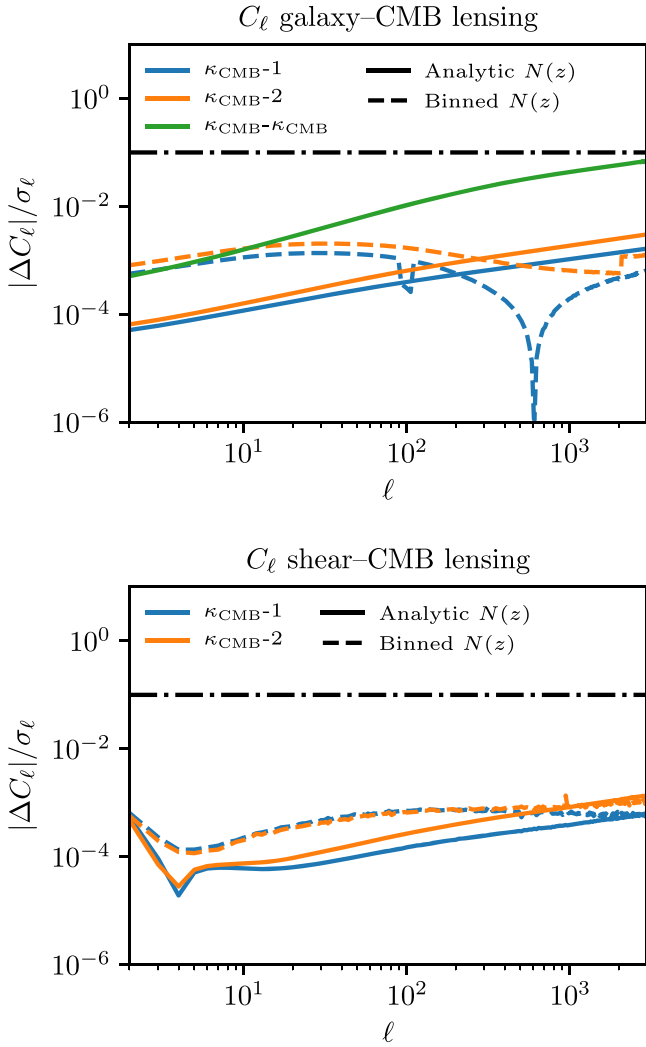
Figure 13. Same as Figure 12 for angular power spectra involving CMB lensing. The black dotted–dashed line indicates the target numerical accuracy of $0.1\sigma_\ell$. Top: cross-correlations with number counts and CMB auto-correlation. Bottom: cross-correlations with weak lensing.

interpolated between $0 < \ell < 6 \times 10^4$ and integrated to obtain the angular correlation function for this observable.

In the case of CMB lensing, we note that the results are particularly sensitive to numerical errors in the computation of the distance to the last scattering surface. The independent code that provides predictions for auto- and cross-correlations of CMB lensing also adopts a different integration strategy from CCL. In this case, integration over redshift is performed via direct summation with a default number of 10 redshift bins. The independent code relies on astropy for constants and background computations, and this difference in implementation can contribute to the discrepancies with CCL.

Cosmological constraints from current weak-lensing surveys are also derived from correlation functions. As we discussed in Section 2, the correlation functions are modeled by Equation (33) and obtained by CCL through numerical integration of predicted angular power spectra. We require that the absolute difference between the CCL prediction and an independent one be smaller than our expected error bars:

$$\mathcal{A} = |\xi^{\mathrm{CCL}} - \xi^{(i)}| < 0.5\sigma_{\mathrm{LSST}}, \qquad (97)$$

where σ_{LSST} is the expected statistical uncertainty of any given correlation function between tracers. The choice of an absolute tolerance criterion here (compared to fractional ones in the previous subsections) is driven by the fact that the correlation function approaches zero at large scales.

To obtain realistic targets for the convergence of projected correlation function computations for LSST analyses, we calculated the expected statistical uncertainty of the clustering and lensing correlation functions of the LSST gold sample (LSST Science Collaboration et al. 2009) assuming an effective source galaxy density of $n_{\mathrm{eff}} = 26\,\mathrm{gal/arcmin}^2$ for galaxy-shape distortions (Chang et al. 2013) and galaxy density of $n_{\mathrm{gold}} = 45\,\mathrm{gal/arcmin}^2$ for number counts. Specifically, we calculated the Gaussian covariance of angular correlation functions following the formalism of Joachimi et al. (2008), and note that leaving out the non-Gaussian covariance terms makes our accuracy criterion more conservative. We split the galaxy samples into 10 tomography bins, defined to contain equal numbers of galaxies.

We compared the difference between CCL and the benchmarks for the cosmic shear, galaxy–galaxy lensing, and galaxy clustering correlations for all tomographic bin combinations and both redshift distributions. Specifically, we took the value of the covariance in the bins centered at $z = 1$ and $z = 1.5$ to compare to the benchmarks. The results of this validation procedure for the projected correlation function are shown in Figures 14 and 15. These suggest that the convergence between CCL predictions and benchmarks is below the expected statistical uncertainty. Similar to the power spectra, we have verified that the target precision is achieved when including intrinsic alignments.

The three-dimensional spatial correlation function $\xi(r)$ predicted by CCL was validated by comparing it with an independent, precise numerical transform.[51] We calculated $\xi(r)$ by transforming the CCL nonlinear halofit power spectrum using this independent method for the five cosmologies listed in Table 3 at redshifts $z = 0, 1, 2, 3, 4,$ and 5. We then compared it with the $\xi(r)$ from CCL with a sampling of $P(k)$ equal to N_K_3DCOR bins per decade. The accuracy metric is defined as

$$\mathcal{A} = |\xi^{\mathrm{CCL}}(r) - \xi^{(i)}(r)|/\xi^{(i)}(r). \qquad (98)$$

The default value of N_K_3DCOR $= 100{,}000$ results in $\mathcal{A} < 2.5 \times 10^{-3}$ for $0.1 < r < 250\,\mathrm{Mpc}$ and $z = 0$. The agreement was better for higher redshifts.

We also compared the absolute value of $r^2\xi(r)$ and find a maximum difference of $\Delta\,(r^2\xi(r)) < 3.0 \times 10^{-2}$ for the range $r = 0.1$–$250\,\mathrm{Mpc}$. This corresponds to approximately 0.08% of the baryon acoustic oscillation peak value of $r^2\xi(r)$. At the peak, the difference is only 9.0×10^{-3}, or 0.024% of the peak height. The results are shown in Figure 16.

To further validate the $P(k) \rightarrow \xi(r)$ transform, we performed a test using an analytical function $\xi(r) = (r/r_0)^a$, whose inverse transform $P(k)$ has a known analytic form, $P(k) \propto k^{3+a}$. We used $r_0 = 5h^{-1}\,\mathrm{Mpc}^{-1}$ and $a = -1.67$, which approximates the actual three-dimensional correlation function. We then compared the CCL calculation of $\xi(r)$ to the known analytic result, defining a metric analogous to Equation (98). This was found to be less than 0.4% in the range $1 < r < 200\,\mathrm{Mpc}$,

---

[51] This independent implementation is based on the cluster toolkit package, available at http://cluster-toolkit.readthedocs.io/en/latest/.
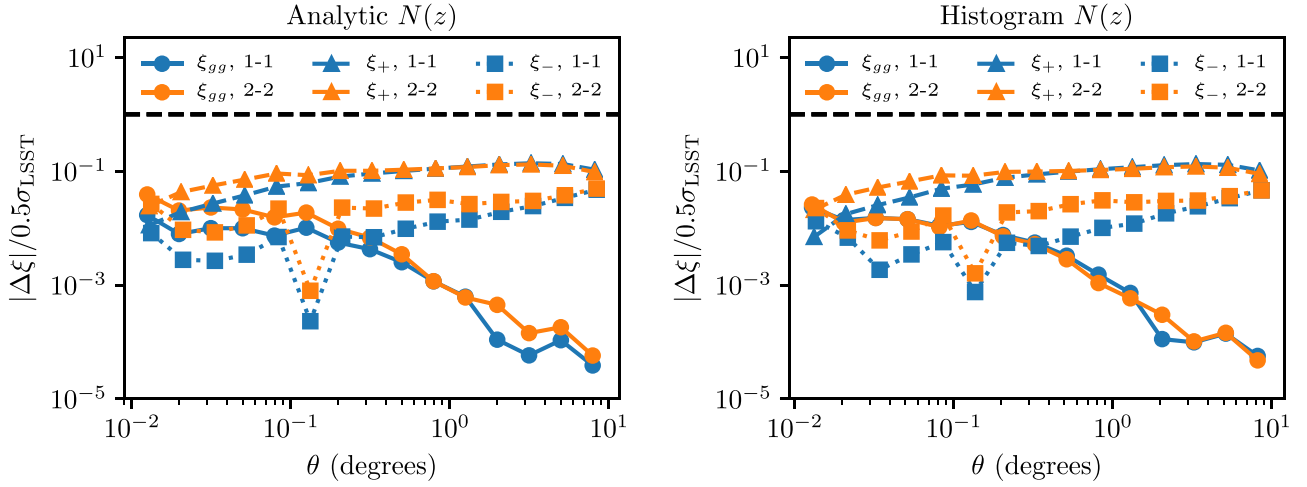
Figure 14. Comparison between the predicted projected correlation functions and the expected uncertainties for LSST. The black dotted–dashed line indicates the target numerical accuracy of $0.5\sigma_{LSST}$. The left panel shows predictions for the analytic redshift distributions, while the right panel shows the case of the redshift histograms. The different markers and colors indicate clustering (ξ_{gg}, Equation (39), filled circles) or lensing ($\xi_{\pm}$, Equation (43), filled triangles and squares) auto-correlations of the 1–1 or 2–2 redshift bin combinations.
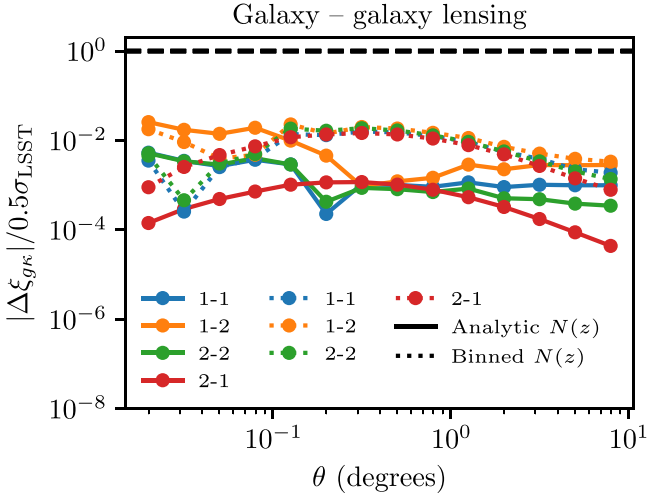
Figure 15. Comparison between the predicted galaxy–galaxy lensing projected correlation function and the expected uncertainty for LSST for both analytic and histogram redshift distributions.

rising to about 5% at $r = 1000\,\mathrm{Mpc}$ (see Figure 17). For $r = 0.1$–$0.8\,\mathrm{Mpc}$, the relative difference is $\approx 8\%$. The accuracy at low and high distances can be improved by increasing the range over which the power spectrum splines are evaluated.

Although this function approximates the true three-dimensional correlation distribution over the range of interest in r, the transform $P(k)$ does not have the correct behavior at low k, where $P(k) \sim k$. Therefore, a second test was performed with the function $P(k) = Ak/(k_0 + k)^4$, where $A = 100$ and $k_0 = 0.045\,\mathrm{Mpc}^{-1}$, which approximates the true behavior of the power spectrum for all k. The transform to $\xi(r)$ was performed using `Mathematica`[52] and compared to the `CCL` calculation. The results, shown in Figure 17, show agreement to within 10^{-4} over most of the range in r. Because this power spectrum results in a correlation function that turns negative at $r \approx 150\,\mathrm{Mpc}$, the accuracy metric is large near this value.

The differences between the `CCL` calculations and the benchmarks are primarily due to the method used to compute the transform of Equation (44). In `CCL`, we use `FFTLog`, while the benchmarks use either a slower precise numerical integration or an exact analytic expression, and therefore differences at the levels observed are not surprising.

`CCL` performs non-Limber computations of angular power spectra through the `Angpow` library as detailed in Section 3.3.2. The `Angpow` software (Campagne et al. 2017a) was tested against `CLASS` and an external brute-force non-Limber implementation, and can perform the same computations approximately an order of magnitude faster ($\mathcal{O}(1s)$). The external code first carried out a brute-force integration of the transfer functions in Equations (22)–(31) using a simple trapezium rule, before computing the integral over k in Equation (21) using an adaptive quadrature method. Its precision and speed parameters were optimized so that the relative numerical difference between the non-Limber computations is lower than two orders of magnitude, from $\ell = 2$ to $\ell = 1000$. We demonstrate this in Figure 18, where we plot the angular clustering power spectrum for a sample of galaxies with $\langle z \rangle = 1$ and a Gaussian redshift distribution that extends between $|z - \langle z \rangle| < 5\sigma_z$, where $\sigma_z = 0.02$, for a CCL1 cosmology. The non-Limber prediction deviates from the Limber case at low l, as expected. The right panel shows the fractional difference between the non-Limber curves, demonstrating the accuracy of the `Angpow` prediction for our choice of precision and speed parameters. Also, the external brute-force non-Limber computation and `Angpow` were tested to recover the Limber-approximated curve at high ℓ for a wide Gaussian window ($\sigma_z = 0.1$). The relative errors with respect to the Limber result at high ℓ are also lower than two orders of magnitudes compared to the expected cosmic variance. The differences between the `CCL` results and benchmarks from `CLASS` can be due to the integration methods and in particular the choice of the integral cutoff for small scales. The `Angpow` implementation in `CCL` sets the k integral cutoff automatically using the user-defined maximum multipole ℓ_{max} as $k_{max} = \pi \ell_{max}/\chi(z_{min})$, where $\chi(z_{min})$ is the minimum comoving distance within the redshift shells, while the `CLASS` user has to set it appropriately.

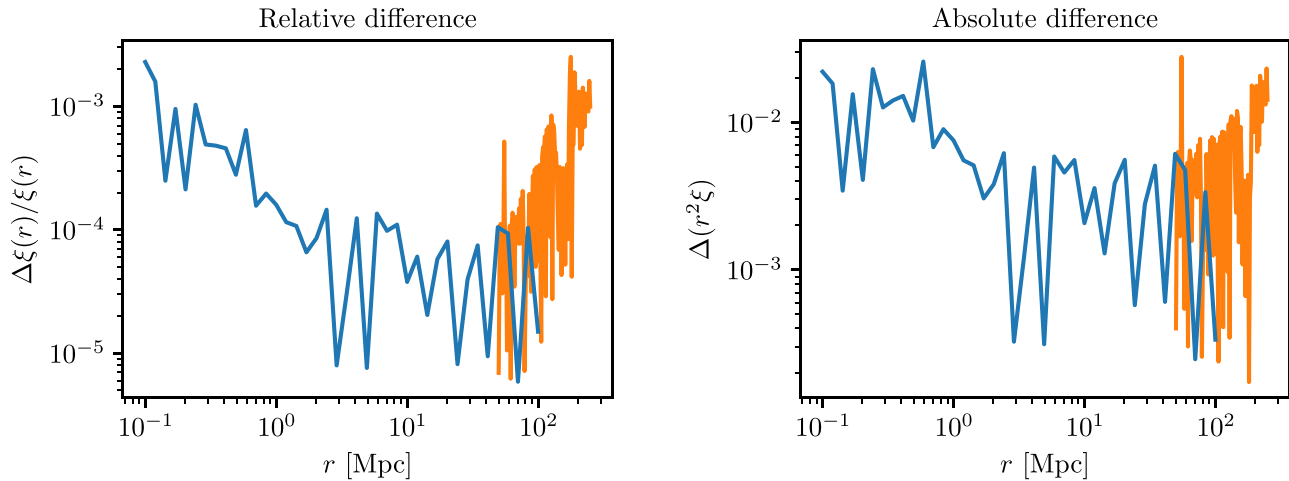[52] http://www.wolfram.com/mathematica/

Figure 16. Comparison of the `CCL` calculation of the three-dimensional spatial correlation function $\xi(r)$ with a precise numerical transform of the `CCL` nonlinear `halofit` power spectrum. The left panel shows the relative error $\Delta\xi(r)/\xi(r)$. The right panel shows the absolute error in $r^2\xi(r)$. Both panels are for the CCL1 model of Table 3 at redshift zero. The comparison is made with 40 points in the range $r = 0.1$–100 Mpc (blue curve) and 100 points in the region $r = 50$–250 Mpc, encompassing the baryon acoustic oscillation peak.
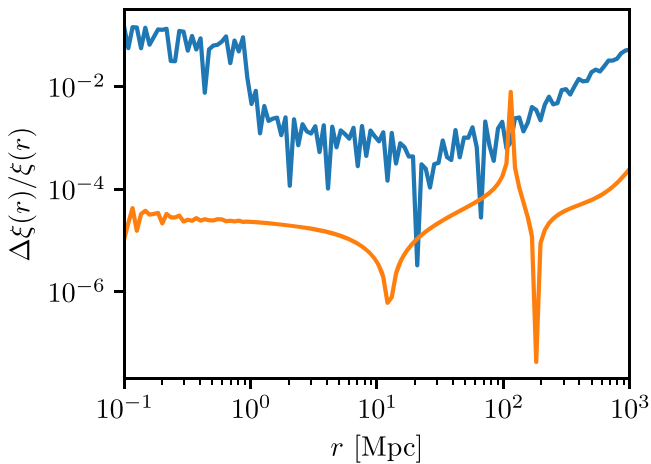
Figure 17. Relative error in the three-dimensional spatial correlation function computed using the `CCL` algorithm compared to an analytic function $\xi(r) = (r/r_0)^{-1.67}$ (blue curve) and using $P(k) = Ak/(k_0 + k)^4$ (orange curve). Both functions have known analytic transforms, $\xi(r)$, but the second one has an asymptotic behavior that matches $P(k) \sim k$ at low k. In this validation test, the known $P(k)$ was transformed with the `CCL` algorithm and compared to the known analytic result for $\xi(r)$.

5. Usage

CCL is a public tool developed by the members of the LSST DESC and can be downloaded from the collaboration's `GitHub` repository.[53] Installation instructions are provided in a README file available in that same repository. In particular, CCL is installable via `pip` with minimal dependencies. These include `cmake`,[54] the GNU Scientific Library,[55] and FFTW3.[56] Instructions on how to generate a Docker[57] image are provided for portability to different architectures.

A suite of tests can be run to ensure installation was successful and all features perform normally. These comprise accuracy checks performed in C and unit tests available in `Python`. These are also run regularly with the `Travis` continuous integration service,[58] ensuring that the code remains reliable as we continue to improve it.

The steps to follow to perform a standard cosmological computation (for example, to obtain angular power spectra for galaxy clustering) in `CCL` are the following:

1. Set up a `cosmology` object which contains all the information on the cosmological model. This will not only specify the values of the cosmological parameters but also the choice of algorithm for computing the matter power spectrum and information on whether to work under a linear approximation. This step already allows the user to compute quantities such as distances, the Hubble rate, or growth functions.

2. In a second step, the user specifies a `tracer` object, which contains all of the information pertaining to the sample of galaxies to be modeled. For galaxy clustering, this includes information on the bias of the sample and its redshift distribution. The `tracer` also contains information on how the clustering is to be modeled, e.g., taking into account magnification effects.

3. Finally, the user can proceed to compute angular power spectra for a given set of multipoles via the function `ccl_angular_cls`, by providing the `tracer` object as input.

An example run corresponding to this case can be found in the `3x2demo` notebook or in the `ccl_sample_run.c` example in the `examples` folder within the repository.

CCL is documented online[59] and through Doxygen[60] files released with the repository. The repository also includes multiple example files in C and several `Jupyter` notebooks showing many common use cases.

CCL is released under terms consistent with BSD 3-Clause licensing.[61]

53 https://github.com/LSSTDESC/CCL
54 http://cmake.org
55 https://www.gnu.org/software/gsl/
56 http://www.fftw.org/
57 https://www.docker.com/

58 https://travis-ci.org
59 https://readthedocs.org/projects/ccl/
60 http://www.doxygen.org/
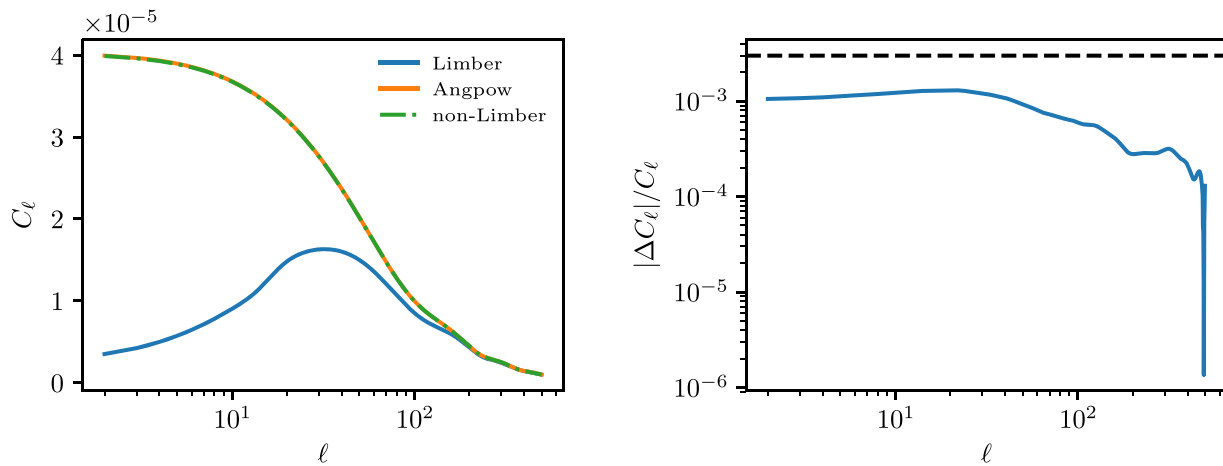61 https://github.com/LSSTDESC/CCL/blob/master/LICENSE

Figure 18. Different predictions for the clustering angular power spectrum of a sample of galaxies with a Gaussian redshift distribution centered on $\langle z \rangle = 1$. The left panel shows the C_ℓ predictions from the Limber case (green), the non-Limber case external to CCL (yellow dotted–dashed), and Angpow (black). The right panel shows the fractional difference in the predicted clustering angular power spectrum between Angpow and the exrternal brute-force non-Limber computation. The relative numerical difference between the non-Limber computations is lower than two orders of magnitude.

6. Outlook

Science software development to facilitate the cosmological inference from LSST data is one of the critical tasks of the DESC. Recent cosmological analyses of the Dark Energy Survey (DES) have relied on CosmoSIS (Zuntz et al. 2014) and CosmoLike (Krause et al. 2017), while analyses of the Kilo Degree Survey (KiDS) have relied on CosmoLSS (Joudaki et al. 2018; based on CosmoMC; Lewis & Bridle 2002) and Monte Python (Audren et al. 2013). All of these frameworks employ CLASS, CAMB (Challinor & Lewis 2005), or the Cosmic Emulator to compute the density power spectra. Compared to the analyses of DES, KiDS and the Hyper-suprime Cam Survey, future data sets (e.g., LSST, Euclid, and *WFIRST*) have substantially higher demands on analysis frameworks. Analyses are becoming more complex in terms of the cosmological physics that is included in the analyses (neutrinos, modified gravity, and dark matter models) and in terms of modeling astrophysical and observational systematics at the required precision.

It is the primary goal of CCL to become the backbone of all cosmological analyses carried out by the LSST-DESC. CCL can also have applications for analytic covariance calculations needed for future analyses of cosmological observables. This unified approach of a validated CCL will ensure that LSST-DESC results are both consistent (in that they will all be based in the same theory framework) and accurate (in that this framework has undergone a rigorous numerical validation).

Within LSST-DESC, the implementation of CCL in realistic analysis pipelines has already begun: all likelihood module prototypes under development use it as its backbone, and the first of these, cosmological analysis of angular galaxy clustering cross-correlations, will serve as a model for the design of the joint-probes likelihood of the LSST-DESC. This work has allowed us to validate the performance of CCL in a realistic analysis scenario, verifying its accuracy and efficiency in the context of computationally demanding Markov Chain Monte Carlo runs.

Beyond its usefulness in the LSST-DESC, the flexible design of CCL makes it an ideal tool for the analysis of other cosmological data sets, as well as for the cross-correlation of different experiments. To this end, and to allow a generic and flexible analysis of the LSST data, further functionality will be added to CCL. Plans are in place to extend the range of standard and nonstandard cosmological models covered by the code, including basic and more complex modified gravity parametrizations (Silvestri et al. 2013; Bellini & Sawicki 2014) and consistent treatment of the growth function and the matter power spectrum in modified gravity theories. Work is already underway to add predictions for cosmology with clusters (McClintock et al. 2019). The simplified treatment of the galaxy–matter connection for galaxy clustering and intrinsic alignments will be improved by implementing generic perturbation-theory approaches to structure formation (McEwen et al. 2016). A more complete implementation of all relevant cross-correlations between large-scale structure observables and other cosmological probes (e.g., CMB -ntegrated Sachs–Wolfe effect—Sachs & Wolfe 1967—and other secondary anisotropies) will also soon be included. Likewise, CCL is expected to provide consistent modeling of complex astrophysical and observational systematics across all probes, critical to LSST analyses.

In general, although this document presents the functionality and performance of CCL shortly after its release, we expect the library to be a continuously evolving piece of software. In particular, we expect to study the trade-offs between numerical accuracy and speed in the future, as well as to propagate the uncertainties in theoretical predictions to a forecasting framework that can determine their impact in cosmological parameters. This will allow CCL to satisfy the analysis needs of future large data sets, as well as more accurate and sophisticated models for a broad range of cosmological and astrophysical observables.

Author contributions are listed below.

Nora Elisa Chisari: co-led project, coordinated hack projects and communication, contributed to: correlation function and power spectrum implementation, documentation, and comparisons with benchmarks.

David Alonso: co-led project; developed structure for angular power spectra; implemented autotools; integrated into LSS pipeline; contributed to: background, power spectrum, mass function, documentation, and benchmarks; reviewed code.

Elisabeth Krause: initiated and co-led project; developed CLASS interface and error handling; contributed to other code; reviewed pull requests.

C. Danielle Leonard: wrote and tested code for LSST specifications, user-defined photo-z interface, and support of neutrinos; reviewed other code; wrote text for this note.

Philip Bull: implemented and documented the Python wrapper; extensive infrastructure work, including maintenance of the build system and unit tests, bug fixes, and code review; enhanced the error handling system; performed power spectrum comparison across parameter space; various architecture/design contributions.

Jérémy Neveu: contributed to Angpow, built the interface with CCL and the comparisons with benchmarks.

Antonio Villarreal: contributed to initial benchmarking, halo mass function code, and general code and issues review.

Sukhdeep Singh: contributed to the correlation functions code and weak-lensing benchmarks.

Thomas McClintock: wrote Python and doxygen documentation.

John Ellison: implemented the 3D correlation function; documentation of 3D correlation function.

Zilong Du: implemented the 3D correlation function.

Joe Zuntz: wrote initial infrastructure, C testing setup, and reviewed code.

Alexander Mead: wrote halo-model code and documentation

Shahab Joudaki: performed benchmarking of angular power spectra and correlation functions for galaxy clustering, galaxy–galaxy lensing, and cosmic shear (including intrinsic alignments); reviewed all CCL benchmarks; contributed to implementation of background functions and documentation.

Christiane S. Lorenz: contributed to accurate high-redshift cosmological background quantities and benchmarked background splines.

Tilman Tröster: wrote code for user-changeable precision parameters and distance tests; found and fixed bugs.

Javier Sanchez: modified setup.py to allow pip installation and uninstall.

Francois Lanusse: contributed to improving installation options.

Mustapha Ishak: contributed to planning of code capabilities and structure; reviewed code; identified bugs and wrote code to fix them; wrote text for this note.

Renée Hlozek: contributed initial code for error handling structures, reviewed other code edits.

Jonathan Blazek: planning capabilities and structure; documentation, review, and testing.

Jean-Eric Campagne: Angpow main builder.

Husni Almoubayyed: reviewed code/contributed to example notebooks and issues.

Tim Eifler: reviewed/tested code.

Matthew Kirby: performed comparison of physical constants.

David Kirkby: writing, testing, and reviewing code. Asking questions.

Stéphane Plaszczynski: contributed to Angpow.

Anže Slosar: wrote and reviewed code.

Michal Vrastil: wrote documentation and example code; reviewed code.

Erika L. Wagoner: set up logarithmic binning in wavenumber.

ORCID iDs

Nora Elisa Chisari ⓘ https://orcid.org/0000-0003-4221-6718
Philip Bull ⓘ https://orcid.org/0000-0001-5668-3101
Antonio Villarreal ⓘ https://orcid.org/0000-0002-8847-0335
Thomas McClintock ⓘ https://orcid.org/0000-0001-8764-5271
John Ellison ⓘ https://orcid.org/0000-0001-8692-9504
Zilong Du ⓘ https://orcid.org/0000-0002-0821-3081
Joe Zuntz ⓘ https://orcid.org/0000-0001-9789-9646
Tilman Tröster ⓘ https://orcid.org/0000-0003-3520-2406
Javier Sanchez ⓘ https://orcid.org/0000-0003-3136-9532
Mustapha Ishak ⓘ https://orcid.org/0000-0002-6024-466X

Jean-Eric Campagne ⓘ https://orcid.org/0000-0002-1590-6927
Matthew Kirby ⓘ https://orcid.org/0000-0002-4788-200X
David Kirkby ⓘ https://orcid.org/0000-0002-8828-5463
Anže Slosar ⓘ https://orcid.org/0000-0002-8713-3695
Erika L. Wagoner ⓘ https://orcid.org/0000-0002-9461-944X

References

Abbott, T. M. C., Abdalla, F. B., Alarcon, A., et al. 2018, PhRvD, 98, 043526
Afshordi, N., Loh, Y.-S., & Strauss, M. A. 2004, PhRvD, 69, 083524
Allison, R., Caucal, P., Calabrese, E., Dunkley, J., & Louis, T. 2015, PhRvD, 92, 123535
Alonso, D., Bull, P., Ferreira, P. G., Maartens, R., & Santos, M. G. 2015, ApJ, 814, 145
Alonso, D., & Ferreira, P. G. 2015, PhRvD, 92, 063525
Angulo, R. E., Springel, V., White, S. D. M., et al. 2012, MNRAS, 426, 2046
Astropy Collaboration, Robitaille, T. P., Tollerud, E. J., et al. 2013, A&A, 558, A33
Audren, B., Lesgourgues, J., Benabed, K., & Prunet, S. 2013, JCAP, 2, 001
Bardeen, J. M., Bond, J. R., Kaiser, N., & Szalay, A. S. 1986, ApJ, 304, 15
Bartelmann, M., & Schneider, P. 2001, PhR, 340, 291
Bellini, E., & Sawicki, I. 2014, JCAP, 7, 050
Beringer, J., Arguin, J. F., Barnett, R. M., et al. 2012, PhRvD, 86, 010001
Blas, D., Lesgourgues, J., & Tram, T. 2011, CLASS: Cosmic Linear Anisotropy Solving System, Astrophysics Source Code Library, ascl:1106.020
Blazek, J., MacCrann, N., Troxel, M. A., & Fang, X. 2017, arXiv:1708.09247
Bonvin, C., & Durrer, R. 2011, PhRvD, 84, 063505
Bryan, G. L., & Norman, M. L. 1998, ApJ, 495, 80
Campagne, J.-E., Neveu, J., & Plaszczynski, S. 2017a, A&A, 602, A72
Campagne, J.-E., Plaszczynski, S., & Neveu, J. 2017b, ApJ, 845, 28
Carroll, S. M. 2001, LRR, 4, 1
Castorina, E., Carbone, C., Bel, J., Sefusatti, E., & Dolag, K. 2015, JCAP, 7, 043
Catelan, P., Kamionkowski, M., & Blandford, R. D. 2001, MNRAS, 320, L7
Challinor, A., & Lewis, A. 2005, PhRvD, 71, 103010
Challinor, A., & Lewis, A. 2011, PhRvD, 84, 043516
Chang, C., Jarvis, M., Jain, B., et al. 2013, MNRAS, 434, 2121
Chevallier, M., & Polarski, D. 2001, IJMPD, 10, 213
Chisari, N. E., Richardson, M. L. A., Devriendt, J., et al. 2018, MNRAS, 480, 3962
Chon, G., Challinor, A., Prunet, S., Hivon, E., & Szapudi, I. 2004, MNRAS, 350, 914
Cooray, A., & Sheth, R. 2002, PhR, 372, 1
Copeland, E. J., Sami, M., & Tsujikawa, S. 2006, IJMPD, 15, 1753
Croton, D. J., Gao, L., & White, S. D. M. 2007, MNRAS, 374, 1303
Dalal, N., Doré, O., Huterer, D., & Shirokov, A. 2008, PhRvD, 77, 123514
Desjacques, V., Jeong, D., & Schmidt, F. 2018, PhR, 733, 1
Desjacques, V., & Seljak, U. 2010, CQGra, 27, 124011
Dodelson, S. 2004, Modern Cosmology (Academic Press: Amsterdam)
Doux, C., Penna-Lima, M., Vitenti, S. D. P., et al. 2018, MNRAS, 480, 5386
Duffy, A. R., Schaye, J., Kay, S. T., & Dalla Vecchia, C. 2008, MNRAS, 390, L64
Durrer, R. 2008, The Cosmic Microwave Background (Cambridge: Cambridge Univ. Press)
Eifler, T., Krause, E., Dodelson, S., et al. 2015, MNRAS, 454, 2451
Eisenstein, D. J., & Hu, W. 1998, ApJ, 496, 605
Feng, J. L. 2010, ARA&A, 48, 495
Frigo, M., & Johnson, S. G. 2012, FFTW: Fastest Fourier Transform in the West, Astrophysics Source Code Library, ascl:1201.015
Gao, L., Springel, V., & White, S. D. M. 2005, MNRAS, 363, L66
Ghosh, B., Durrer, R., & Sellentin, E. 2018, JCAP, 06, 008
Giocoli, C., Bartelmann, M., Sheth, R. K., & Cacciato, M. 2010, MNRAS, 408, 300
Green, J., Schechter, P., Baltay, C., et al. 2011, arXiv:1108.1374
Hamilton, A. J. S. 2000, MNRAS, 312, 257
Heitmann, K., Bingham, D., Lawrence, E., et al. 2016, ApJ, 820, 108
Hellwing, W. A., Schaller, M., Frenk, C. S., et al. 2016, MNRAS, 461, L11

Hildebrandt, H., Viola, M., Heymans, C., et al. 2017, MNRAS, 465, 1454
Hirata, C. M., Mandelbaum, R., Ishak, M., et al. 2007, MNRAS, 381, 1197
Hirata, C. M., & Seljak, U. 2004, PhRvD, 70, 063526
Ishak, M. 2007, FoPh, 37, 1470
Joachimi, B., & Bridle, S. L. 2010, A&A, 523, A1
Joachimi, B., Schneider, P., & Eifler, T. 2008, A&A, 477, 43
Joudaki, S., Blake, C., Johnson, A., et al. 2018, MNRAS, 474, 4894
Kamionkowski, M., & Spergel, D. N. 1994, ApJ, 432, 7
Kitching, T. D., & Heavens, A. F. 2017, PhRvD, 95, 063522
Krause, E., Eifler, T., & Blazek, J. 2016, MNRAS, 456, 207
Krause, E., Eifler, T. F., Zuntz, J., et al. 2017, arXiv:1706.09359
Lattanzi, M., & Gerbino, M. 2017, arXiv:1712.07109
Laureijs, R., Amiaux, J., Arduini, S., et al. 2011, arXiv:1110.3193
Lawrence, E., Heitmann, K., Kwan, J., et al. 2017, ApJ, 847, 50
Lesgourgues, J., & Pastor, S. 2012, AdHEP, 2012, 608515
Lewis, A., & Bridle, S. 2002, PhRvD, 66, 103511
Limber, D. N. 1954, ApJ, 119, 655
Linder, E. V. 2003, PhRvL, 90, 091301
LSST Dark Energy Science Collaboration 2012, arXiv:1211.0310
LSST Science Collaboration, Abell, P. A., Allison, J., et al. 2009, arXiv:0912.0201
Mamajek, E. E., Prsa, A., Torres, G., et al. 2015, arXiv:1510.07674
Mao, Y.-Y., Zentner, A. R., & Wechsler, R. H. 2018, MNRAS, 474, 5143
McClintock, T., Varga, T. N., Gruen, D., et al. 2019, MNRAS, 482, 1352
McEwen, J. E., Fang, X., Hirata, C. M., & Blazek, J. A. 2016, JCAP, 9, 015
Mead, A. J., Peacock, J. A., Heymans, C., Joudaki, S., & Heavens, A. F. 2015, MNRAS, 454, 1958
Mo, H. J., & White, S. D. M. 1996, MNRAS, 282, 347
Mohammed, I., & Gnedin, N. Y. 2017, arXiv:1707.02332
Mohammed, I., & Seljak, U. 2014, MNRAS, 445, 3382
Mohr, P. J., Newell, D. B., & Taylor, B. N. 2016, RvMP, 88, 035009
Nakamura, T. T., & Suto, Y. 1997, PThPh, 97, 49
Navarro, J. F., Frenk, C. S., & White, S. D. M. 1997, ApJ, 490, 493
Ng, K.-W., & Liu, G.-C. 1999, IJMPD, 8, 61
Padmanabhan, T. 2003, PhR, 380, 235
Paranjape, A. 2014, PhRvD, 90, 023520
Parfrey, K., Hui, L., & Sheth, R. K. 2011, PhRvD, 83, 063511
Peacock, J. A. 1999, Cosmological Physics (Cambridge: Cambridge Univ. Press)
Peacock, J. A., & Smith, R. E. 2000, MNRAS, 318, 1144
Peebles, P. J., & Ratra, B. 2003, RvMP, 75, 559
Porter, T. A., Johnson, R. P., & Graham, P. W. 2011, ARA&A, 49, 155
Reinecke, M. 2011, A&A, 526, A108
Sachs, R. K., & Wolfe, A. M. 1967, ApJ, 147, 73
Schneider, A., & Teyssier, R. 2015, JCAP, 12, 049
Schulz, A. E., & White, M. 2006, APh, 25, 172
Seljak, U. 2000, MNRAS, 318, 203
Semboloni, E., Hoekstra, H., & Schaye, J. 2013, MNRAS, 434, 148
Semboloni, E., Hoekstra, H., Schaye, J., van Daalen, M. P., & McCarthy, I. G. 2011, MNRAS, 417, 2020
Sheth, R. K., Mo, H. J., & Tormen, G. 2001, MNRAS, 323, 1
Sheth, R. K., & Tormen, G. 1999, MNRAS, 308, 119
Silvestri, A., Pogosian, L., & Buniy, R. V. 2013, PhRvD, 87, 104015
Singh, S., Mandelbaum, R., & More, S. 2015, MNRAS, 450, 2195
Smith, R. E., & Markovic, K. 2011, PhRvD, 84, 063507
Smith, R. E., Peacock, J. A., Jenkins, A., et al. 2003, MNRAS, 341, 1311
Smith, R. E., Scoccimarro, R., & Sheth, R. K. 2007, PhRvD, 75, 063512
Springel, V., Pakmor, R., Pillepich, A., et al. 2018, MNRAS, 475, 676
Sugiyama, N. 1995, ApJS, 100, 281
Sunayama, T., Hearin, A. P., Padmanabhan, N., & Leauthaud, A. 2016, MNRAS, 458, 1510
Takahashi, R., Sato, M., Nishimichi, T., Taruya, A., & Oguri, M. 2012, ApJ, 761, 152
Talman, J. 2009, CoPhC, 180, 332
Tinker, J., Kravtsov, A. V., Klypin, A., et al. 2008, ApJ, 688, 709
Tinker, J. L., Robertson, B. E., Kravtsov, A. V., et al. 2010, ApJ, 724, 878
Troxel, M. A., & Ishak, M. 2015, PhR, 558, 1
Upadhye, A., Biswas, R., Pope, A., et al. 2014, PhRvD, 89, 103515
van Daalen, M. P., Schaye, J., Booth, C. M., & Dalla Vecchia, C. 2011, MNRAS, 415, 3649
van Uitert, E., Joachimi, B., Joudaki, S., et al. 2018, MNRAS, 476, 4662
Villarreal, A. S., Zentner, A. R., Mao, Y.-Y., et al. 2017, MNRAS, 472, 1088

Vogelsberger, M., Genel, S., Springel, V., et al. 2014, Natur, 509, 177
Watson, W. A., Iliev, I. T., D'Aloisio, A., et al. 2013, MNRAS, 433, 1230
Weinberg, D. H., Mortonson, M. J., Eisenstein, D. J., et al. 2013, PhR, 530, 87
Wong, Y. Y. Y. 2011, ARNPS, 61, 69
Yoo, J. 2010, PhRvD, 82, 083508
Yoo, J., Fitzpatrick, A. L., & Zaldarriaga, M. 2009, PhRvD, 80, 083514

Zaldarriaga, M., & Seljak, U. 1997, PhRvD, 55, 1830
Zhao, G.-B., Saito, S., Percival, W. J., et al. 2013, MNRAS, 436, 2038
Zumalacárregui, M., Bellini, E., Sawicki, I., Lesgourgues, J., & Ferreira, P. G. 2017, JCAP, 8, 019
Zuntz, J., Paterno, M., Jennings, E., et al. 2014, CosmoSIS: Cosmological parameter estimation, Astrophysics Source Code Library, ascl:1409.012
Zuntz, J., Paterno, M., Jennings, E., et al. 2015, A&C, 12, 45